The Suzaku High Resolution X-Ray Spectrometer

Richard L. KELLEY[1], Kazuhisa MITSUDA[2], Christine A. ALLEN[1], Petar ARSENOVIC[1],
Michael D. AUDLEY[3], Thomas G. BIALAS[1], Kevin R. BOYCE[1], Robert F. BOYLE[1],
Susan R. BREON[1], Gregory V. BROWN[4], Jean COTTAM[1], Michael J. DIPIRRO[1],
Ryuichi FUJIMOTO[2], Tae FURUSHO[2], Keith C. GENDREAU[1], Gene G. GOCHAR[1],
Oscar GONZALEZ[1], Masayuki HIRABAYASHI[5], Stephen S. HOLT[6], Hajime INOUE[2],
Manabu ISHIDA[7], Yoshitaka ISHISAKI[7], Carol S. JONES[1], Ritva KESKI-KUHA[1],
Caroline A. KILBOURNE[1], Dan MCCAMMON[8], Umeyo MORITA[7], S. Harvey MOSELEY[1],
Brent MOTT[1], Katsuhiro NARASAKI[5], Yoshiaki OGAWARA[2], Takaya OHASHI[7],
Naomi OTA[9], John S. PANEK[1], F. Scott PORTER[1], Peter J. SHIRRON[1],
Gary A. SNEIDERMAN[1], Andrew E. SZYMKOWIAK[10], Yoh TAKEI[2], June L. TVEEKREM[1],
Stephen M. VOLZ[11], Mikio YAMAMOTO[12], and Noriko Y. YAMASAKI[2]

[1]*NASA/Goddard Space Flight Center, Greenbelt MD 20771, USA*
Richard.L.Kelley@gsfc.nasa.gov
[2]*Institute of Space and Astronautical Science (ISAS), Japan Aerospace Exploration Agency (JAXA),*
3-1-1 Yoshinodai, Sagamihara, Kanagawa 229-8510
[3]*UK Astronomy Technology Centre, Royal Observatory, Blackford Hill, Edinburgh, EH9 3HJ, UK*
[4]*Lawrence Livermore National Laboratory, 7000 East Ave., L-260, Livermore, CA, 94550, USA*
[5]*Space Cryogenic Systems, Quantum and Advanced Equipment Division,*
Sumitomo Heavy Industries, Ltd., 5-2 Soubiraki-cho, Niihama, Ehime
[6]*Olin College, someplace in MA, zipcode, USA*
[7]*Department of Physics, Tokyo Metropolitan University, Minami-Osawa 1-1,*
Hachioji-shi, Tokyo 192-0397
[8]*Department of Physics, University of Wisconsin, Madison, WI 53706, USA*
[9]*RIKEN, 2-1 Hirosawa, Wako, Saitama 351-0198*
[10]*Department of Physics, Yale University, New Haven, CT zipcode, USA*
[11]*NASA Headquarters, 300 E. St. SW, Washington, DC 20546-0001, USA*
[12]*Miyazaki Univeristy, 1-1 Gakuen Kibanadai-nishi, Miyazaki 889-2192*

(Received 2006 August 32; accepted 2006 September 31)

Abstract

The high resolution X-Ray Spectrometer (XRS) has been designed to provide the *Suzaku* Observatory with very high spectral resolution, non-dispersive spectroscopy from 0.3 to 12 keV. This energy range encompasses the most diagnostically-rich part of the x-ray band. The sensor consists of a 32 channel array of x-ray of microcalorimeters, each with an energy resolution of about 6 eV. The very low temperature required for operation of the array (60 mK) is provided by a four-stage cooling system containing a single stage ADR, superfluid He Cryostat, solid Ne Dewar, and a single-stage Stirling-cycle cooler. The *Suzaku*/XRS is the first orbiting x-ray microcalorimeter spectrometer and has been designed to last more than three years in orbit. The early verification phase of the mission demonstrated that the instrument was working properly and that the cryogen consumption rate was low enough to ensure a mission lifetime exceeding 3 years. However, the liquid He cryogen was completely vaporized two weeks after opening the dewar guard vacuum vent. The problem has been traced to inadequate venting of the dewar He and Ne gases out of the spacecraft into space. In this paper we present the design of the XRS instrument and describe the in-flight performance.

Key words: instrumentation: detectors—X-rays: general

1. Introduction

Over the last decade there has been a revolution in the observational capabilities for studying celestial x-ray sources. Imaging, spectroscopic and collecting area performance have improved dramatically through missions such as ROSAT, ASCA, *Chandra*, and XMM-Newton. These x-ray observatories have led to a large number of discoveries with significant implications and relevance throughout astrophysics and cosmology. Along with the tremendous progress that has been made in developing high resolution x-ray optics with increasing collecting areas (e.g., ROSAT; Serlemitsos et al. 1995; Jansen et al. 2001; Weisskopf et al. 2002; ARE THESE OK?), a key component leading to the enormous progress has been the increase in capabilities for high resolution x-ray spectroscopy. Thus far, high spectral resolution, defined here as several eV, has utilized dispersive spectroscopy, including Bragg spectrometers and transmission and reflection gratings. These devices offer very high spectral resolution for energies below about 1 keV (e.g., Canizares et al. 2000; Brinkman et al. 2000; den Herder et al. 2001), but the spectral resolving power decreases toward higher energies and the resolution degrades with increasing solid angle. Non-dispersive, photon-counting spectrometers have provided astrophysicists with powerful capabilities for moderate spectral resolution, but with high spatial resolution, with CCD's being the best example (e.g., Germire 1999; Strüder et al. 2001; Turner et al. 2001; Koyama et al. 2006). However, these devices all use charge collection as the essential detection element and have Fano-limited spectral resolution well below what can be achieved with dispersive spectrometers.

Starting in 1982, with the anticipated plans to develop the AXAF observatory (now *Chandra*), members of this team embarked on new ways to utilize semiconductors with energy band gaps smaller than Si or Ge to improve the energy resolution by increasing the number of electrons per event. This enquiry led to the idea of the thermal detection of x-ray photons, using principles and techniques well-know in infrared astronomy. The tremendous potential of the calorimetric approach was quickly realized by Moseley, Mather, McCammon (1982), who developed the concept and demonstrated that a resolution in the electron volt range was possible with semiconductor thermometers and small pixels (<mm^2) operating below $\sim$ 100 mK. The microcalorimeter can be made to have high quantum efficiency over a large energy band along with nearly constant energy resolution. The spectral resolving power thus increases toward high energies, making it an ideal complement to the dispersive spectrometers. Further, an array of microcalorimeters can be used to create an imaging spectrometer for the study of extended sources. This makes the sensor particularly powerful for the diagnostic capabilities for elements heavier than Si, and especially the ubiquitous Fe K lines, including high-precision velocity sensitivity. Following proof-of-principle work and a proposal to implement a microcalorimeter spectrometer for the AXAF observatory, the high resolution X-Ray Spectrometer (XRS) was eventually selected for flight development. For the next seven years or so, substantial progress was made on the detectors and cryogenic system required for maintaining the detector below 100 mK for several years in orbit.

In 1993, after a restructuring of the NASA AXAF program, and plans in Japan to develop a powerful new x-ray observatory, it was mutually decided by NASA and the Institute of Space and Astronautical Science (ISAS) to incorporate the XRS into the Astro-E mission. The XRS would provide the high spectral resolution for the mission, complementing the grating spectrometers on *Chandra* and XMM-Newton (figures 1 and 2), while the other instruments on Astro-E would provide larger field of view and collecting area (the XIS; Koyama et al. 2006) and extend the bandpass to very high energies with much higher sensitivity (the HXD; Takahashi et al. 2006b). The XIS would also continue to operate after the cryogens of the XRS were exhausted, enabling imaging with moderate spectral resolution for the full life of the mission. Within about a year the XRS was redesigned and a new version emerged based on a joint design with major components to be contributed by NASA and ISAS. By 1999 the instrument was completed and ready for flight on Astro-E. Following the loss of the Astro-E during launch, proposals were successfully made to the respective national space agencies to rebuild the observatory and the instruments for a new mission, Astro-E2. This mission has now been successfully launched, renamed *Suzaku*, and is currently in operation carrying out observations proposed from around the world (Mitsuda et al. 2006).

With the *Suzaku*/XRS now in orbit, a new era begins for a technology capable of unprecedented spectral sensitivity over a broad energy band. The subject of this paper is the design, ground testing and in-flight performance of the XRS instrument. Before describing the XRS, however, we very briefly continue the history and mention other work that is ongoing that utilizes microcalorimeter technology for both astrophysics and related laboratory work. In

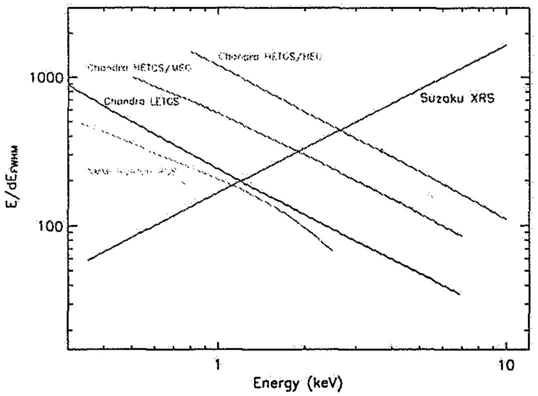

Fig. 1. Spectral resolving power of the XRS in comparison with *Chandra* and XMM-Newton, the currently operating x-ray observatories that are capable of high resolution x-ray spectroscopy. The missions utilize gratings that provide very high resolution at low energies, which the non-dispersive aspect of the microcalorimeter enables increasing resolving power toward high energies.

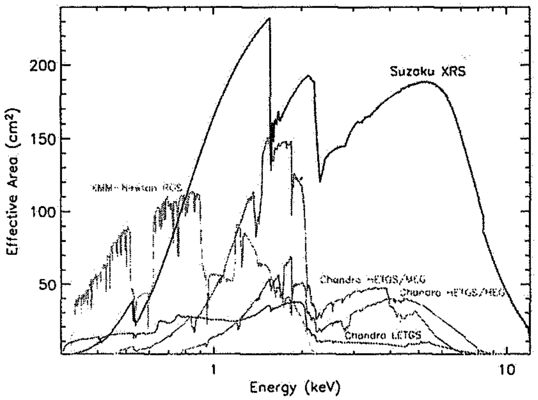

Fig. 2. Effective area of the XRS in comparison with the *Chandra* and XMM-Newton. The high intrinsic quantum efficiency of the microcalorimeter, coupled with the large throughput of the *Suzaku* X-Ray Telescope (Serlemitsos et al. 2006), provide large effective area for enabling high sensitivity spectroscopy.

parallel with the development of the XRS, work was begun in the early 1990's on a suborbital payload to measure the spectrum of the diffuse x-ray background below about 1 keV. This payload, the X-Ray Quantum Calorimeter (XQC), has been flown several times and has produced the first celestial x-ray spectrum with a microcalorimeter (McCammon et al. 2002). More recently, members of this team and other groups have used x-ray calorimeter technology for laboratory work, in including atomic and nuclear physics, using electron-beam ion traps (refs). Based on the success of this technology, and now the operation of the XRS microcalorimeter in space, much larger missions are being formulated that will have much larger arrays, enabled further by alternate thermometer and read out schemes, that should permit much larger fields of view. These include the Japanese New X-ray Telescope (NeXT; Takahashi et al. 2006a), the NASA Constellation-X Mission (ref) and the ESA/JAXA XEUS mission (e.g., Bavdaz et al. 2004).

2. Instrument Overview

The concept underlying the microcalorimeter is based on the very definition of energy - the energy of light (or particle) quanta are inferred from the temperature increase of a thermometer in quasi-static equilibrium with an absorbing heat capacity. A thermometer scheme commonly used is the temperature-dependant resistance of a doped semiconductor or superconductor operated in its phase transition. At very low temperatures ($\lesssim 0.1$ K), the heat capacity, Johnson noise of the thermistor and thermal fluctuations ("phonon noise") between the sensor and heat sink can be made low enough that the amplitudes of heat pulses from individual x-rays can be sensed to better than a part in a thousand (Moseley et al. 1982; Stahle et al. 1999; McCammon 2005). Real devices have varying limitations, such as additional noise terms associated with the particular fabrication or choice of materials, position-dependant response, and the limited availability of materials that thermalize X-ray efficiently without contributing excessive heat capacity. However, it is possible to quantify these non-ideal effects and design a detector that is optimized for a particular energy resolution and quantum efficiency. The goal of the XRS was to produce a microcalorimeter array with an energy resolution of 12 eV or better at 6 keV in order to allow nearly complete resolution of the "triplet" line complex of He-like iron as a primary goal. The necessity for an array of microcalorimeters was set by the requirement to cover a useful field of view (~ 10 arcmin^2) yet remain within a heat capacity budget low enough to permit this resolution. Over a period of about a decade, work centered on producing devices that have this resolution with a high degree of uniformity over an array of 32 individual microcalorimeter pixels with size ~ 0.4 mm^2. For the XRS, the most straightforward path toward this was to use micromachined silicon as the basis of the array, with ion-implanted Si as the thermometer (i.e., a thermistor), and use the semi-metallic crystal mercury telluride (HgTe) as the x-ray absorber (refs).

The implementation of a microcalorimeter spectrometer for *Suzaku* required a robust cooling system capable of cooling the sensor to 60 mK for a period of at least 2 years in order to carry out a comprehensive scientific observing program. This required a cryogenic system with extremely low heat loads and also fit within a volume of $\lesssim 1$ m^3. To meet these constraints, a three stage cooling system was developed jointly by Goddard, the University of Wisconsin, ISAS, and the Sumitomo Heavy Industries, Ltd. (SHI). Figure 3 shows a diagram of the major components of the XRS.

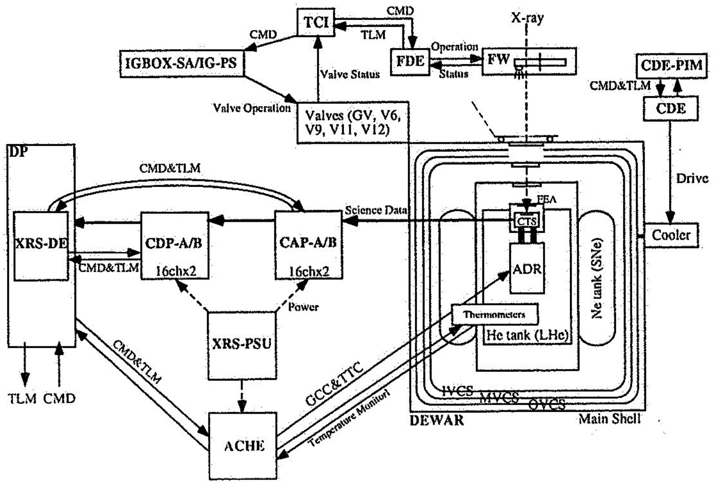

Fig. 3. XRS subsystem functional block diagram

The detectors are cooled to the operating temperature with a conventional single stage adiabatic demagnetization refrigerator (ADR; e.g., Serlemitsos et al. 1990). The ADR is suspended within a 1 T A^{-1} superconducting magnet that is immersed in a 32 liter liquid He Cryostat. The He bath is pumped by space to about 1.3 K (hence below the superfluid transition temperature of 2.2K) and provides the heat sink for the ADR. To achieve the design requirement of a 2 year lifetime (and possibly the goal of 3 years), the net heat load into the He Cryostat of was required to be less than 1.2 mW assuming the Cryostat is 90% full at the beginning of the mission. To reduce the external heat loads on the helium, the Cryostat is mounted within a ~ 120 liter toroidal dewar that contains solid neon, which is also be space-pumped to a temperature of about 17 K. Careful attention to thermal isolation, controlling superfluid film creep, heat sinking and staging of components to minimize parasitic heat loads was required simultaneously with the need to keep the system as modular as possible, and survive the demanding launch loads of the M-V rocket. The He Insert, consisting of the He Cryostat, ADR, detector assembly, blocking filters and instrument electronics were the responsibility of Goddard. The University of Wisconsin supplied the flight ADR salt pill. The Ne Dewar, including Stirling-cycle mechanical cooler, was developed at SHI under the direction of ISAS. The other electronics boxes (power and telemetry/commanding) were provided through ISAS, and the Filter Wheel was developed at the Tokyo Metropolitan University and ISAS. The ground calibration of the instrument was done primarily at Goddard with assistance from ISAS.

The microcalorimeters are by their nature highly sensitive to essentially all forms of electromagnetic and particle radiation, so proper isolation from structures at higher temperature was necessary. This required the development of aluminized plastic filters that are thin enough to transmit x-rays yet strong enough to survive a few torr of differential pressure, repeated thermal cycling to cryogenic temperatures, and substantial random mechanical vibration and shock loads.

As described in detail below, an resolution of 6 eV was achieved during pre-launch tests and a resolution of 7 eV was obtained in orbit. The slight degradation is due to the effects of cosmic rays perturbing the temperature of the Si frame of the array. In the following sections we will successively go through the major components of the XRS, starting with the detector array and ending up with the electronics, and then discuss the performance of the XRS.

3. XRS Detector System

3.1. The Microcalorimeter Array

The XRS microcalorimeter array is based on ion-implanted Si for the thermometer. The Si is implanted to a value just below the metal-insulator transition in order to achieve a very high temperature coefficient of resistance at low temperatures. Etching of silicon is used to form the thermally isolating support beams to the heat sink. Finally, HgTe is manually attached to each pixel to absorb and thermalize x-rays. Discussion of the development of the *Suzaku*/XRS array design can be found in Stahle et al. (2003), and details of the new fabrication process are found in Brekosky et al. (2004). In this paper, we provide a brief description of the design and fabrication method.

The process starts with a silicon-on-insulator (SOI) wafer, which consists of a thin layer of silicon separated from the bulk silicon substrate of the wafer by a very thin oxide buffer. This buried oxide serves as both an etch stop and a diffusion barrier. Reactive-ion etching (RIE) is used to create thermally-isolated pixels. RIE is a dry etch process that permits the etching of silicon into any desired shape which can be defined by means of photolithography. Deep RIE equipment allows silicon etching with nearly straight side walls through a 400 μm wafer to create deep wells behind each detector array element. A photolithographically patterned structural polymer is used to create a controlled interface between the implanted Si and the absorber. Nano^{TM}SU-8, a structural polymer sold by MicroChem, enabled the design of precise absorber attachment points for improved resolution uniformity from pixel to pixel.

The thermistor was formed by doping with phosphorus (P) compensated with boron (B). The thickness of the top silicon layer of an SOI wafer determined the thermistor depth. After capping with an oxide, we implanted a single dose each of P and of B into the 1.5 μm-thick SOI layer. After annealing at high temperature to remove implanting damage and locate the ions at substitutional lattice sites, a uniform doping density throughout the 1.5 μm depth was achieved. We eliminated the effects of lateral diffusion by implanting over an area larger than the thermistor area and then defining the thermistor edges with the etch. We used degenerately doped leads to contact the thermistor. A lower density implant was used on the membrane in order to limit the heat capacity of the thermal sensor; a heavier dose was used on the solid frame. The room-temperature resistivity of the lighter dose was $\sim 200\ \Omega$/square, and the heavier was $12\ \Omega$/square. The resistivities drop by less than a factor of 2 on cooling to 4 K.

The combination of SOI and RIE enabled the fabrication of silicon links of the desired thermal conductance and minimum resonant frequency while maintaining a compact design. Though the thermal conductance achieved in the flight design was about a factor of two higher than expected from scaling from measurements of straight beams fabricated on previous generations of devices, the conductance was uniform across pixels, across arrays, and across different fabrication runs. The resulting exponential decay time was 3–4 ms, depending on bias. The finite thermal conductance of the link between absorber and thermistor contributed to this time constant; modeling indicated a fall time of 2 ms would have resulted with perfect thermal coupling between the absorber and thermistor.

For the absorber attachment points we developed a way to form 10 μm thick spacers made of SU-8 on each pixel. Due to a concern that applying epoxy or SU-8 directly to the thin silicon of the thermistor element could result in strain-induced changes in its electrical properties, we added tabs to the edges of each thermistor and placed cylindrical spacers on the tabs. Figure 4 shows an optical image of an individual pixel with an electron micrograph inset of an SU-8 spacer. There are four per pixel. A benefit of this attachment technique is that the line response has been greatly inproved compared with previous techniques that had the absorber, or an intermediate spacer, attached directly to the thermistor volume. Each pixel now has a nearly perfect Gaussian response to monochromatic x-rays. An example of the line shape is shown in figure 5.

There is a small penalty for this attachment scheme, however. The thermal conductance between the absorber and the thermistor is nearly the same as that between the whole calorimeter and the heat sink. This degrades the signal-to-noise ratio because the detector response falls more steeply at high frequencies than the thermal fluctuation noise associated with the link to the heat sink. The internal thermal fluctuation noise that also results from this decoupling is

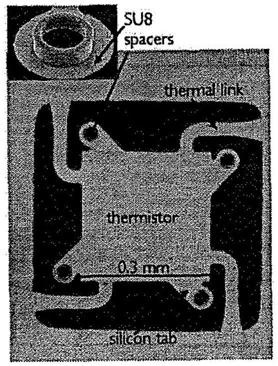

Fig. 4. Photos of a single XRS microcalorimeter thermometer. The square section is implanted to form the thermistor. There are four support beams and also four absorber "tabs" on which the HgTe absorbers are subsequently attached. The thermistor area and support beams are 1.5 μm thick.

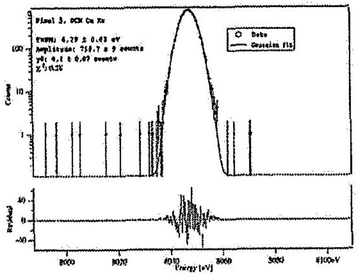

Fig. 5. XRS line spread function on a single pixel as obtained using x-rays from an x-ray monochromator tuned to Cu Kα.

not a factor because it is less than the Johnson noise at the sensitivity of the XRS detector. The range in pulse risetimes across the XRS array corresponds to $\pm \sim 30\%$ variation in the absorber-thermistor thermal conductance, and slightly higher resolution is clearly correlated with the faster risetimes. Modeling detector response across that range in risetimes predicts energy resolution ranging from 4.5 eV to 5.2 eV, compared with 4 eV if the absorber were perfectly coupled to the thermistor. The remaining difference between the predicted resolution and the measured resolution of typically 6 eV appears to be due to the thermal noise from x-rays hitting other pixels and the silicon around the array, which we will address later in this section.

The HgTe was grown by DRS Infrared Technologies on CdZnTe wafers using molecular beam epitaxy. We removed the CdZnTe substrate completely using a wet etch, leaving free HgTe foils that we diced mechanically to the appropriate size. We measured the heat capacity of our 624 μm × 624 μm × 8.5 μm HgTe absorbers as a function of temperature, and found $C(T) = 0.10(T/0.1\ \mathrm{K}) + 0.11(T/0.1\ \mathrm{K})^3$ pJ K^{-1}. The cubic term is consistent with a Debye temperature of 140 K. We attribute the linear term to an electronic heat capacity resulting from defects in the HgTe. The presence of Hg vacancies, for example, causes a p-type doping of the material and an associated electronic heat capacity term. This excess heat capacity equals the Debye term at ~ 0.1 K and is twice the Debye term at our biased operating point of ~ 0.074 K.

To attach the absorbers to the SU-8 tubes, we applied Emerson and Cummings Stycast$^{\mathrm{TM}}$1266 epoxy to the upper interior of each of the 4 tubes per pixel using a straight section of 12 μm stainless steel wire mounted to a fixture attached to an XYZ micron positioner stage. The size of epoxy was gauged by the wire size; the epoxy sphere diameter could be up to twice the wire diameter. The wire was inserted into the SU-8 tube and removed, leaving the top of the tube filled. We used vacuum tweezers attached to an XYZ-tilt stage to maneuver each absorber into position. Figure 6 shows the completed array. The pixels of the central 6 × 6 array have a 640 μm pitch. At the corner of the 12 × 14 mm detector chip is a pair of additional devices nominally identical to those in the array. These are situated outside of the aperture. A collimated x-ray source was pointed at one of them so that it could serve as gain scale monitor. When changes in gain are the result of drift in the heat sink temperature, the gain history of a single pixel can be used to correct the gain of the entire array. The use of a collimated x-ray source and a dedicated calibration pixel makes it possible to achieve a low background at the main array. We instrumented 30 array channels and one calibration pixel.

3.2. Performance and Characteristics of the Microcalorimeter Array

On four arrays assembled, the resolution of the various pixels ranged from 5.3–6.5 eV FWHM, nearly independently of energy, except for 1–2 pixels per array. The resolution of those pixels for low-energy photons was similar to the rest of the pixels, but they degraded

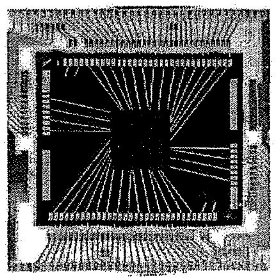

Fig. 6. Completed microcalorimeter array. The array consists of 36 pixels that are 624 μm × 624 μm. Of these, 32 are read out in flight - 31 on the array and a calibration pixel located on the bottom right, which is out of the telescope field of view. The typical gap size between the pixels is 15 μm, so the filling factor is about 95%.

Table 1. Detector parameters determined from fits of a representative pixel (at biased operating point of 74 mK)

Parameter	Value
heat capacity C of absorber (HgTe)	0.11 pJ K^{-1}
thermal conductance G between absorber and thermistor	61 pW K^{-1}
heat capacity C of thermistor	0.07 pJ K^{-1}
thermal conductance G between thermistor and heat sink	60 pW K^{-1}
$\alpha \equiv d\log R/d\log T$	−7.005
resistance R at operating point	27.3 MΩ
effective time constant $\tau_{\rm eff}$ (for total C, G to heatsink, and α)	2.2 *ms*
Actual fall time (slowed by G between absorber and thermistor)	3.5 ms

more rapidly with energy. The characteristics of the array are summarized in tables 1 and 2. For flight operations, the detector system is biased to 2 V using the circuit shown in section 3.4. This leads to the operating resistance given in table 1.

Table 2. Absorption efficiency of the HgTe.

HgTe properties	Value
mean areal density and 1σ deviation	69.2 ± 1 μg mm^{-2}
theoretical 6 keV absorption efficiency	0.969 ± 0.0015
nominal fraction of unit cell covered	$(0.624/0.640)^2 = 0.951$
combined efficiency	0.92

Despite the excellent performance, there were several unexpected features of the microcalorimeter array that became apparent in ground testing. The ground testing allowed preparation for these effects in orbit, and preliminary indications from the limited in-orbit data indicate that the prepared procedures would have succeeded. The effects were differential gain changes, background events due to cosmic ray interaction in the thick frame of the device, and count-rate dependent noise.

The principle behind using a dedicated calibration pixel is that all pixels experience the same relative change in gain. It was expected that changes in the temperature of the warmer parts of the cryostat could, via conduction and radiation, change the temperature gradient between the control thermometer and the actual detector heat sink or change the bolometric loading of the pixels, but that such effects would act on all pixels in the same way. What we found instead was that the calibration pixel responded more sensitively to changes in the neon and helium temperatures than did any pixel in the array, and that the outer pixels of the array were more sensitive than the inner pixels. A variety of possible causes were considered, but the pattern of sensitivity, with the calibration pixel being the most sensitive, invalidated most proposed mechanisms. One possibility still under consideration is differential absorbed power due to screening from surrounding pixels. The level of absorbed power is on the scale of tens of femto-watts; if it were uniform it would have no impact on detector performance. Due to the differential sensitivity, however, gain correction based on the calibration pixel would overcorrect the gain of the pixels in the scientific array. We planned, in orbit, to make frequent use of the filter wheel position with calibration sources (see section 7 for details) in order to quantify the scale of the problem in normal operation (instead of just after cryogen transfers). Future calorimeter assemblies will be designed to reduce further the amount of long-wavelength radiation that can get into the detector enclosure.

We observe frequent groupings of nearly simultaneous pulses (time spans of hundreds of micro-seconds, based on time tags assigned by the CDP) on many pixels. We know from a variety of ground tests, including irradiation with alpha particles, that such events occur when an impulse of energy is deposited into the frame of the calorimeter chip and causes a pulse in the frame temperature. We will refer to the occurrence of such simultaneous pulses as a "frame event". Most frame events are low energy. A minimum ionizing particle going the shortest way through the frame deposits 150 keV into the silicon of the frame and makes pulses on multiple pixels that look like ~ 50 eV photons. Frame events amplify the apparent background rate because the area of the frame is 13 times the area of the biased pixels, and because each cosmic ray on the frame makes pulses on most of the pixels in the array. Because the cooling time for the frame is similar to the risetime for real x-ray events, the pulses produced in frame events are not easily distinguished from x-ray events based only on pulse shape. Thus, rejection based on coincidence was required. Ground background data were analyzed in order to determine a screening algorithm based on the intervals between pulses, the number of pixels involved, and the pulse heights.

An effect related to frame events is count-rate dependent noise. When an x-ray is absorbed in the frame, the resulting frame-event pulses are too small to trigger, but they add to the noise of each pixel. Additionally, when a photon is absorbed in one pixel and that heat flows to the frame, a similar perturbation in the frame temperature occurs. This thermal crosstalk has been measured directly for gamma-rays, but for x-rays it just adds to the noise. These two terms combine to make resolution depend on the photon flux and spectrum incident over the entire XRS aperture; the extra noise scales as $\Sigma_E \sqrt{N(E)E^2}$, where $N(E)$ is the number of photons at energy E. We determined a degradation function from ground calibration data, using data from inner pixels, outer pixels, and the calibration pixel in order to separate the effects of crosstalk from that of x-rays hitting the frame. In practice, this noise would have affected only observations of the brightest sources; we anticipated that the resolution of the inner pixels would degrade to ~ 9 eV for an observation of a point source with a power-law spectrum with a flux of 10^{-8} erg s^{-1} cm^{-2} and unity photon index. In section 10.2.1 we show how this sensitivity affected the energy resolution in flight, due to the effects of cosmic ray heat deposition in the Si frame of the array. Both the count-rate dependence of the resolution and the frame events can be eliminated in future designs by improving the heat sinking of the array.

3.3. The Anti-coincidence Detector

Because a fraction of cosmic rays that traverse the calorimeter pixels will leave behind energy comparable to photons in the XRS spectral bandwidth, an anti-coincidence detector was implemented both to reject cosmic ray events and to be a rapidly responding witness of the particle environment. We chose to employ a silicon ionization detector rather than another calorimeter in order to provide a faster signal with temperature invariant gain that could provide diagnostic information in the event of signal saturation on the calorimeter array. The XRS anti-coincidence detector was designed to operate at the calorimeter heat sink temperature at low (< 9 V) bias so that it could be placed directly behind the calorimeter array. The sensor itself is a very simple design. The chip consists of 1 $\mathrm{cm}^2 \times 0.5$ mm of high purity silicon (nominally 13–21 kΩ cm at room temperature). One surface is degenerately doped with phosphorus (n+) while the other is degenerately doped with boron (p+), and both sides are metalized with aluminum. Thus it is configured as a p-i-n diode and is operated with the standard reverse-bias relative to that configuration. The device should not be considered a diode at an operating temperature of ~ 60 mK, however, because the carriers in the central intrinsic region are completely frozen out and the detector is simply an insulator between metallic contacts. Biases up to 24 V were investigated. No change in gain was seen for biases above 2 V. The XRS anti-coincidence detector was biased at 6 V using the circuit shown in figure 7 (section 3.4).

We patterned the contacts so that their edges were 0.15 mm from the physical edge of the chip, which was itself defined by DRIE. The corners of both the physical and the electrical perimeter were rounded. Thus we eliminated uncontrolled field-concentrating features and a possible break-down path along dicing-induced surface states at the edge. The performance was otherwise unchanged.

In flight operation, the pulse spectrum of the anti-coincidence detector is not accumulated. Rather, the signal is compared to a commandable threshold, and if the signal exceeds that threshold during a time window associated with each calorimeter pulse, then the calorimeter signal is flagged. The energy equivalent of the 1σ value of the voltage noise was 1.6 keV. The default threshold was 16 keV, which was well below the 195 keV deposited by a minimum ionizing particle traversing 0.5 mm of Si.

The calorimeter array was mounted on an alumina board that was placed directly on top of the anti-coincidence detector board, with the anti-coincidence detector itself fitting in a hole in the array board. The top surface of the particle detector sits 0.63 mm below the plane of the calorimeter pixels. Considering an isotropic flux of minimum-ionizing particles, 98% of those impacting the calorimeter array will pass through the anti-coincidence detector. Those that miss tend to have longer path lengths in the HgTe absorbers, enhancing their rejection based on their being out of the observational band. Using a GEANT[1] model, we determined that less than 0.1% of all incident minimum ionizing particles will deposit energy in the calorimeter of less than 10 keV without triggering the anti-coincidence detector (Saab et al. 2004). An attempt was also made to model the unrejected background from secondary particles. The resulting prediction, though larger than that calculated for direct interaction of primary cosmic rays only, was less than that expected from scaling from the ASCA SIS background (Gendreau 1995), which was itself less than what was observed in orbit. The underestimate is presumed due to the low-fidelity model used to describe the surrounding structure and from the failure to include all the relevant interactions in the simulation.

3.4. Microcalorimeter Detector Assembly.

FEA design section goes here...

4. Liquid He Cryostat .

The He Cryostat serves as the mechanical and thermal interface for the detector and ADR assembly (Shirron et al. 2006). It was designed as a self-contained unit that is inserted into the Ne Dewar with plumbing, electrical, mechanical and thermal interfaces only at the front end. The interfaces have been simplified to fill and vent line connections, electrical connectors, and mounting flexures for structural support. This added to the complexity of the Cryostat's front end layout and assembly, but ensured that all components critical to its performance were fully tested prior to delivery to Japan for integration.

Within mass and space allocations, the cryogen volume could not be much larger than about 30 liters, which translated to a maximum time average heat load of approximately 1 mW

---

[1] http://geant4.web.cern.ch/geant4/.

Fig. 7. Detector bias circuit.

in order to meet the 3-year lifetime goal. This was roughly two orders of magnitude smaller than any previous superfluid helium dewar built for space, and required a far more careful assessment of heat loads. As a result, the XRS He Cryostat pioneered several new technologies that enable it, and future dewars, to meet such stringent cooling requirements.

The He Insert, shown in figure 8, consists of a 34.2 liter aluminum He tank supported inside a cylindrical titanium shell by 12 graphite/epoxy straps, the ADR and detector assembly, and valves, plumbing and phase separator to support fill and vent operations. The ADR is inserted into the front end of the He tank so that the magnet's windings are immersed in superfluid, and the mounting flange has an indium seal to the He tank. Heat from the ADR is absorbed either directly from the magnet's windings or the mounting flange. The fill and vent system has a specially designed porous plug phase separator that ensures 100% utilization of all venting helium, and the network of plumbing includes two heat exchangers along the vent line to provide maximum benefit from vapor cooling.

With such a complex and interdependent system, there are a multitude of trade studies that could be, and many were, performed. As an example, one of most important arose from the strong dependence of the ADR's average heat load on He tank temperature. The ADR benefits from a colder heat sink through lower parasitic heat loads and larger cooling capacity. That, in turn, reduces the frequency of recycling and the total heat rejected each time. The trade-off is that lower temperatures can be achieved only through increased plumbing sizes - with correspondingly higher conducted heat loads - and changes to the phase separator and vent which could allow helium to escape as a liquid. Since many of these trades had to be completed before all dependencies were known, the final design is not necessarily fully optimized. Nevertheless, the design met the 3-year lifetime goal, and with sufficient ($\sim 30\%$) margin to allow critical components such as the high-T_c current leads to be fully redundant.

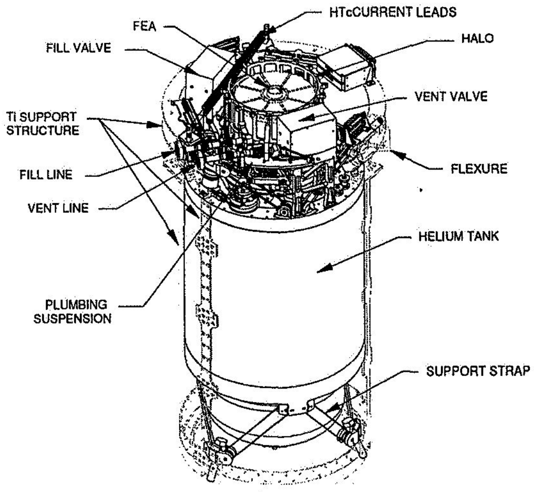

Fig. 8. Schematic of the XRS He Insert, consisting primarily of the He Cryostat, ADR, and detector assembly. The Insert was designed to be modular and have simple interfaces to the Ne Dewar. The light green portion of the drawing outlines the titanium support structure, which is essentially a cylinder from which the He Cryostat is suspended. The top-to-bottom length is n cm and the mass is n kg.

4.1. He Tank and Titanium Support Structure

The He tank is fabricated from aluminum cylindrical sections welded to machined aluminum heads. The He tank is contoured so that it, the 6 forward and 6 aft straps fit completely inside the titanium cylindrical shell that provides a uniform 17 K environment. The smallest gap between the He tank and shell is 1 cm. Titanium is used for strength, so the entire assembly can be cantilevered off the Ne tank using mounting flexures at the forward end. The straps are graphite/epoxy, and all are configured to provide both axial and tangential constraints on tank position. There are three attachment points on the He tank at each end (120° apart), and 3 on the shell at each end, offset from the He tank by 60°. Pairs of straps originate at each attachment point on the He tank and angle outward to the two closest attachment points on the Ti shell. This configuration achieves the required structural rigidity needed for launch on an M-V rocket with the lowest parasitic heat leak.

The straps at the forward end are shorter than those at the aft end because of the access to vapor cooling nodes at the front end of the He tank. The "warm" and "cold" heat exchangers in the vent line run at approximately 11 K and 3 K, under equilibrium flow conditions, and a system of copper wire heat straps thermally connects the 6 forward straps to these heat exchangers at optimal points along their length. Because of the distance and the difficulty of suspending straps along the He tank, vapor cooling the 6 aft straps would have had marginal benefit, and was therefore not done.

Radiative heat loads were minimized by coating and/or polishing the low temperature surfaces. Both the He and Ne tanks were highly polished, and the titanium shell was electroplated with gold. Radiative loads were not directly measured, but since they are one of the dominant heat sources, they could be estimated from measurements of the total load and knowledge of other individual loads. The estimates were consistent with the assumed emissivity of 0.05 for these surfaces.

4.2. Dewar Guard Vacuum

The need to avoid even extremely small heat loads on the He Insert prompted the installation of a carbon/carbon composite getter on the He tank. While there was no anticipated source of helium that could contaminate the guard vacuum, residual pressures as low as 10^{-8} torr - beyond the range of available gauges - would result in a heat leak of 25 μW from 17 K. The getter's surface area could accommodate 1.5 standard liters of helium gas at a pressure of less than 10^{-8} torr.

4.3. Fill and Vent Lines

The fill and vent lines, and fluid control valves, use a fairly standard configuration. Each line attaches to the He tank via a stepper-motor controlled valve, and there is a similar valve located on the Ne tank that, when opened, allows helium to bypass the He tank. This is used for precooling the lines before a fill or topoff operation. The vent line also has a porous plug phase separator in parallel with its valve. The fill line is mechanically and thermally anchored to the vent line at the warm and cold heat exchangers. The penetrations to the He tank are located so the Dewar can be filled and operated in both horizontal and vertical orientations, and such that the He tank can theoretically be filled to 97% (of 34.2 liters) when vertical, as it is on the launch pad.

The final topoff of the Dewar before launch is performed with a supply dewar containing helium just above the superfluid transition, and the flight He tank pumped to ~ 1.3 K. The goal is to end with the flight Dewar as close to full as possible with helium as cold as possible. For three topoff procedures (1 dry run, and 2 pre-launch fills), all achieved 100% fill levels (of the maximum accessible volume of 33.1 liters) at 1.9–2.17 K. Lower temperatures were achieved when the transfer was terminated immediately on reaching 100%. In the best case, the final volume after continued pumping was 30.56 liters (92.3%) remaining after pumping down to 1.21 K.

4.4. Porous Plug Vent System

The phase separator used to retain liquid in the He tank while releasing boiloff vapor is based on "porous plugs" used successfully on previous space missions, but with modifications that prevent the loss of helium through film flow. Porous plug (PP) phase separators were first developed for the IRAS mission (Neugebauer et al. 1984), and use a plug of sintered stainless steel bonded into the vent line. The pores are typically a few μm in diameter, and stainless steel is used because of its relatively poor thermal conductivity. Under normal conditions, liquid in the He tank wets and fills the plug, and the lower pressure in the vent line causes evaporation on its downstream side. This sets up a temperature gradient which, in superfluid helium, also sets up a pressure gradient - known as the thermomechanical effect - which exceeds the difference in saturated vapor pressure on the two sides of the PP. The result is a net pressure acting to push liquid back through the PP into the He tank. This is usually balanced by surface tension, so that liquid is present on the downstream side of the PP and the temperature difference across it is on the order of a few mK.

In addition to the flow of helium through evaporation, there will be a flow of film from the perimeter of the PP. The flow is driven by van der Waals forces, and is constrained only by the superfluid critical velocity, v_c. For saturated films, v_c is inversely proportional to thickness, yielding the curious property that mass flow ($\rho_s v_c d$, where ρ_s is the superfluid density and d is the film thickness) is essentially constant, regardless of temperature and pressure. It is proportional to the (smallest) diameter of the vent line, and is equivalent to a cooling loss of 1.24 mW per cm since the latent heat of the helium is not extracted from the remaining liquid. For typical sizes, ~ 1 cm, this would exceed the total heat budget for the He dewar. A re-analysis of PP data from previous missions showed excess helium vent rates of exactly this magnitude, but it was not recognized at the time since the dewars had average heat loads of 100 mW or more. It should be noted that while film's latent heat is lost, it does contribute to vapor cooling. This can offset as much as 30% of the loss, but for XRS this would still be catastrophic.

The solution was to use a relatively small porous plug and to thermally anchor a small diameter vent line to the He tank just downstream of the PP. [A schematic drawing or photo would be very helpful.] The PP was sized to have a temperature drop of approximately 40–50 mK at the nominal flow rate of 40 $\mu\mathrm{g\,s^{-1}}$. As the venting vapor and film heat exchange with the He tank, warming by 30–40 mK, the film is completely evaporated and heat is extracted from the He tank.

4.5. High-T_c Current Leads

A particular challenge for XRS was the need for currents in the range of 0.5 to 2 A to run the ADR's magnet and the stepper-motor valves. Since both of these are mission critical and at times critical to safe operation, it was prudent to make their electrical leads fully redundant.

With very limited vapor cooling available, normal metal leads could not be used to span the 17 K to 1.3 K gap, but using high-T_c superconductor leads posed the dual problem of fabricating leads sized for this current range, and providing structural support for the fragile leads without adding excessive thermal conductance. In the end, two different superconducting technologies and lead assemblies were used.

For the XRS, there are two high-T_c lead assemblies wires in parallel for redundancy. The first assembly uses 12 YBCO filaments, each capable of carrying at least 10 A, bonded to the outside of a thin tube of G-10. The tube was formed from a layer of cloth impregnated with epoxy, and was supported by Kevlar rope strung along the center of the tube and attached to two G-10 washers bonded inside near the ends. In this way, the tube and filaments were not under any preload and needed to support only their own weight during accelerations. The filaments transitioned to niobium-titanium (NbTi) wires at the cold end, with the joint thermally anchored to the cold heat exchanger (at ~ 3 K). The heat conducted through the assembly from 17 K to the cold heat exchanger was 175 μW, and conduction to 1.3 K, through the NbTi wires, was negligible.

The second assembly uses 12 MgB_2 wires inside Teflon insulation [We should say that the MgB_2 is actually in stainless stell tubing oprivided by Goldacker and his group.]. To our knowledge, this is the first time this recently identified superconductor (Nagamatsu et al. 2001) has been used in space. The wires were bonded to the outside of two G-10 washers located roughly 1/3 of the way in from each end. This assembly was also supported by Kevlar rope attached to the G-10 washers, which were thermally anchored to the hot and cold heat exchangers on the vent line. The solder connections to NbTi wire at the cold end were anchored to the He tank. The conductance of this assembly was significantly higher than for the YBCO set (870 μW to the cold heat exchanger and 34 μW to 1.3 K), but an earlier problem with the heat exchanger warming while current was flowing and causing NbTi leads to burn out justified having redundant leads that were not affected by this warming. [INCLUDE PHOTO OF HIGH-CURRENT LEADS.]

4.6. Adiabatic Demagnetization Refrigerator

A single-stage ADR was used to physically support and cool the detector array to the operating temperature of 60 mK. The ADR consisted of a 920 g ferric ammonium alum (FAA) "salt pill" in a 2 T NbTi magnet connected to the helium bath through an active gas-gap heat switch (GGHS). The switch used a zeolite getter that, when cold, would adsorb the approximately 10 standard cm^3 of ^{3}He gas and open the switch, and when warmed above 13 K would release enough gas to close the switch. The magnet was specially designed to produce 2 T with a current of just under 2 A. It included extensive shield and bucking coils to zero out the dipole moment. This was both to limit the fringing field in the vicinity of the detectors and JFET amplifiers, and to minimize interference with spacecraft components such as magnetic torquers.

The heat switch directly connects the salt pill to an interface plate so that the assembly can be inserted into the magnet bore and thermally connected to the bath by bolting the plate to the magnet. The salt pill is thus physically cantilevered off the interface plate. This is accomplished by a suspension system consisting of a thin titanium shell (similar in function to the one surrounding the He tank) surrounding the salt pill, with end caps that support a network of Kevlar ropes that center the salt pill within the titanium shell. The end cap at the front end is fastened to the interface plate. The heat switch is a structural member in this assembly, mainly providing an axial constraint on the salt pill. The gap between the titanium shell and the magnet bore is small, and there is certainly incidental contact. However, the suspension system is designed to hold the salt pill against launch loads even without this additional support.

For operation at 60 mK, FAA has the highest cooling capacity of common ADR refrigerants. The 2 T field achieves optimal entropy suppression of approximately 50% at the bath temperature, and yields a cooling capacity of 0.42 J at 60 mK. This will support a heat load of 4.9 μW for the required 24 hour hold time. The combined parasitic heat leak through the heat switch and Kevlar suspension is 3.0 μW, and dissipation from the detectors (mainly conduction through the detector lead wires) is approximately 1 μW. Consequently, the ADR can hold the detectors at temperature for close to 30 hours. [IT WOULD BE USEFUL TO HAVE THE HEAT SWITCH ON-CONDUCTANCE AND THE PARASITIC HEAT LOAD WHEN OFF. IT WOULD ALSO BE USEFUL TO HAVE A SCHEMATIC OF THE ADR OVERALL AND HEAT SWITCH.]

Recycling the ADR is accomplished by 1) ramping the magnetic field, causing the salt pill to warm above the bath temperature, 2) closing the heat switch and continuing the ramp to full field, 3) waiting until the salt pill cools to 1.35 K, and then opening the heat switch, and 4) ramping the magnetic field down to cool the detectors to 60 mK. In step 2, the ramp rate is regulated to keep the salt pill from warming above 1.8 K. This was done to minimize the total amount of heat transferred to the helium bath, which comes from three main sources: hysteresis heat from the magnet, heat used to warm the getter to activate the heat switch, and heat from the salt pill. Magnet hysteresis heat depends only on the field excursion, not on the rate or duration. Heat from the getter depends on the amount of time the switch is closed, so more aggressive magnetization rates will reduce the total. However, the heat generated by the salt pill is proportional to its temperature during magnetization, and this favors less aggressive rates. As it is, the total heat produced per cycle is approximately 25 J (6 from magnet hysteresis, 16 from the salt pill, and 3 from the getter heater), and the time required to recycle is less than 1 hour.

4.7. He Cryostat Thermal Model and Performance

We describe test results of the He Cryostat performance conducted from 2004 February 16–March 2. Leak checks were made using the Alcatel 142 helium leak detector. Room temperature leak checks were performed on the Cryostat by alternately filling the He tank with gaseous helium at one atmosphere and pumping it out to see any difference in the leak detector background of 1.5×10^{-8} std. $\mathrm{cm}^3\,\mathrm{s}^{-1}$. Using data logging to look at fine detail, we were able to determine that there were no leaks at a level of 1×10^{-10} std. $\mathrm{cm}^3\,\mathrm{s}^{-1}$ or higher. After warm up to room temperature on March 5, another check of the ^{4}He background in the vacuum space was made which gave similar results. The ^{3}He signal was less than 6×10^{-8} std. $\mathrm{cm}^3\,\mathrm{s}^{-1}$ at room temperature and $< 4 \times 10^{-9}$ std. $\mathrm{cm}^3\,\mathrm{s}^{-1}$ at 60 K ($< 3 \times 10^{-7}$ std. $\mathrm{cm}^3\,\mathrm{s}^{-1}$ was the requirement).

After the Cryostat was cooled to approximately 70 K, the ^{4}He leak checks were repeated. Again, no leaks were seen with a resolution of better than 1×10^{-10} std. $\mathrm{cm}^3\,\mathrm{s}^{-1}$ against a background of 1.3×10^{-8} std. $\mathrm{cm}^3\,\mathrm{s}^{-1}$. This contrasts with measurements in 2003 October with the known leak in the vent line resulting in a leak indication using the same technique of 2×10^{-8} std. $\mathrm{cm}^3\,\mathrm{s}^{-1}$, a factor of more than 200 higher.

A room temperature check of ^{3}He signal in the vacuum space was made to verify that the ADR heat switch was not leaking or permeating ^{3}He at an unacceptable rate. The resulting measurement of 6×10^{-8} std. $\mathrm{cm}^3\,\mathrm{s}^{-1}$ was judged as consistent with previous room temperature measurements. During warm up, with the insert at 60 K the ^{3}He signal was measured again and found to be less than 4×10^{-9} std. $\mathrm{cm}^3\,\mathrm{s}^{-1}$. The required leak rate is $< 3 \times 10^{-7}$ std. $\mathrm{cm}^3\,\mathrm{s}^{-1}$ for a full heat switch under all conditions (warm and cold). These readings from the switch are consistent with results performed in other test dewars. Note that the higher room temperature reading dropped dramatically (factor of 10) when a condensing surface, such as a tank filled with LN_2 was present. No LN_2 was present during in the XRS Test Dewar when the 6×10^{-8} std. $\mathrm{cm}^3\,\mathrm{s}^{-1}$ measurement was made.

There are two vertical and one diagonal level detectors used for ground operations. The diagonal level detector reads values only above ∼ 53%, but this is within the range required for redundancy for the low temperature top-off, the only critical level detector operation. The two superconducting liquid level detectors (LLDs) were checked for function at 4.2 and superfluid temperatures. The vertical LLD performed nominally with a "zero" reading at around 2% and a smoothly varying fill level indication up to 100%. The diagonal LLD did not give a reading below ∼ 53% even with no liquid in the He tank, indicating a shorted heater in the lower level detector. It operated nominally above this fill level. The LLDs are for ground use only. In particular, they are very important for the low temperature top-off operation just before launch. For this operation the diagonal LLD is fully functional with critical levels only occurring above 60% full.

The two Astro-E2 XRS cold valves operated without problems both at 4.2 K and superfluid temperatures. The fill valve when closed is leak tight to at least 1.6×10^{-6} std. $\mathrm{cm}^3\,\mathrm{s}^{-1}$ (requirement $< 1 \times 10^{-4}$ std. $\mathrm{cm}^3\,\mathrm{s}^{-1}$). The fill valve was cycled (closed then opened) two times and the vent valve was cycled 3 times with no anomalous behavior in either the valve actuation itself (nominal 1 A current and 20 s actuation time) or in heating of the cold heat sink where the high current leads that connect the valves to the outside are heat stationed. Note that about 35 J are dissipated into the He tank each time a valve is operated. This leads to a response in temperature both on the He tank and on the cold heat exchanger. In addition, when the vent valve is closed, the vapor cooling is immediately diminished. This leads to an increased temperature on the cold heat exchanger. These effects are all expected and normal.

Table 3. XRS mass gauge test results

mass gauge	initial temperature [K]	final temperature [K]	heat pulse [J]	full volume [liter]	result [liter]
1	1.455738	1.459465	8.92	32.3	15.09
2	1.457277	1.460891	8.92	32.3	15.56
3	1.19322	1.20437	8.92	32.3	15.58

The second time that the fill valve was closed, the fill line from the valve out to and including the Test Dewar plumbing to room temperature was evacuated and put on a leak detector. With 4.2 K vapor on the upstream side of the fill valve, the leak detector background was below 1.6×10^{-6} std. $\mathrm{cm}^3\,\mathrm{s}^{-1}$, indicating no leak bigger than this value through the seat of the fill valve. This is much better than the requirement of no more than 1×10^{-4} std. $\mathrm{cm}^3\,\mathrm{s}^{-1}$ through the valve seat. The vent valve cannot be check in this way due to presence of the porous plug in parallel. Indirectly, through the parasitic heat load test, it was verified that no large flow exists through the vent valve seat.

We have determined that the XRS mass gauge system meets the accuracy requirement of 5% of full volume.

The duration of the mass gauging heat pulse was 100.0 s, the constant current over this time was 4.88 mA and the mass gauge heater resistance was 3746.15 Ω. This gives a heat pulse of 8.92 J. The test data are shown in table 3. These differ by 3%, but only by 1.5% of the full volume. Note that initial and final temperatures given are corrected for self heating offset and for fore and after drift slopes to the center of the mass gauging heat pulse.

The amount of liquid in the He tank as determined by a liquid level detector reading was 14.9 ± 0.5 liters so the errors in the three values were +0.19, +0.66, and +0.68 liters or 0.6%, 2.0%, and 2.1% of full volume, well within the required accuracy.

The porous plug and heat exchanger behaved nominally. Results matched earlier component tests and Insert performance tests from 2003 July.

The porous plug and heat exchanger assembly was tested the cold vent valve closed and with the Test Dewar tilted to 70° in order to wet the porous plug with superfluid. The flow rate through the porous plug was varied by throttling external GSE valves. The temperature

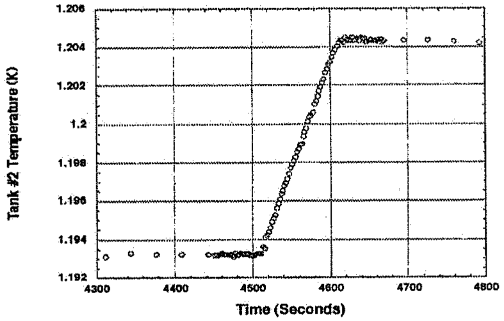

Fig. 9. Results of Mass Gauge #3 as shown on He Tank #2 thermometer. The fore drift and after drift slopes are given more accurately by He Tank #1 which uses a higher excitation (1 nA as opposed to 10 nA), but also sufferer from self heating so is not used to determine the absolute value of the tank temperature.

of the porous plug and the flow rates as measured on the Hastings mass flow meter were recorded at several points of decreasing flow rate. The data matched earlier measurements of the components and in the prior performance test in 2003 July (figure 10).

In addition, during the parasitic heat load test (see next section), the equilibrium temperature of the He tank was lowered from 1.3 K to 1.23 K. This resulted in a lower parasitic load, which can be completely explained by the earlier porous plug and heat exchanger tests. These results confirm that no excess superfluid film is escaping the heat exchanger.

4.8. *He Cryostat Heat Loads*

The Cryostat parasitic heat loads (JFETs on but no ADR operation) under the boundary condition of a 17 K Ne tank temperature were measured. The result of 903 μW is close to the 880 μW predicted by the model. This compares with 711 μW for Astro-E XRS with a similar boundary condition. The difference appears to be mainly due to the higher conductance of the MgB_2 leads than the redundant YBCO leads of Astro-E XRS (75%) and the support strap heat sink locations (15%) with the remainder of unknown origin.

The heat flow is measured by volume flow rate of helium gas pumped out of the Cryostat vent line and through a Hastings mass flow meter and a wet test meter in series. The volume flow is converted to mass flow rate using temperature and pressure corrections and the ideal gas law. The temperature of the He tank is required to be extremely stable during these tests (< 0.25 mK h^{-1} required with a goal of < 0.1 mK h^{-1}) so that only small corrections due to net heat flow into or out of the liquid need be made. In our final measurements we achieved drift rates of 0.02 and 0.06 mK h^{-1} with a result that less than 10 μW is attributable to this net heat.

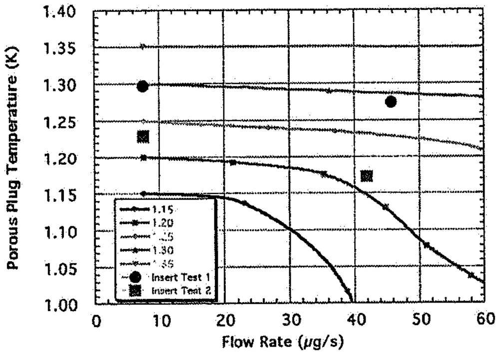

Fig. 10. Comparison of component test of porous plug assembly (lines) with Tests in Insert (large circles and squares). The component tests were performed with simulated tank temperatures ranging from 1.15 K to 1.35 K. It is seen that the Insert Test results, which were done at slightly different temperatures than the component tests, are consistent with the curves of the component tests.

In addition, the effect of the porous plug temperature drop and heat exchanger effectiveness was determined by changing the operating temperature of the He tank. The 903 ± 20 μW (the error bar is due to accuracy rather than resolution of the measurement) was measured with the He tank at 1.228 K and the porous plug at 1.172 K. When measured with the He tank at 1.297 K and the porous plug at 1.275 K, the parasitic heat was 996 μW. The difference is due to the small amount of film flow leakage when the temperature difference across the porous plug and heat exchanger is less than 40 mK. The expected temperature on orbit is 1.21 K (see section 4.10) so the lower heat flow number is more correct. Note that to calculate the heat of vaporization, and hence the heat load in microwatts and the lifetime in years, the temperature used is the He tank temperature and not the porous plug exit temperature. This is because the heat exchanger not only evaporates the residual superfluid film at the He tank temperature, but also thermalizes the boil off gas, thus recovering the higher heat of vaporization (and slightly more!) of the He tank temperature. For example, the latent heat of vaporization at 1.228 K is 21.51 J g^{-1}. At 1.172 K it is 21.26 J g^{-1}. However, the change in enthalpy of the gas going from the porous plug temperature of 1.172 K to the heat exchanger at 1.228 K is 0.27 J g^{-1}, more

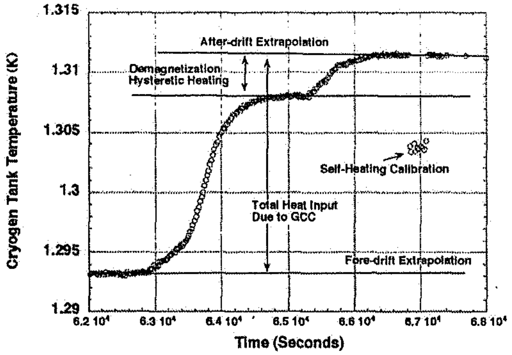

Fig. 11. Calorimetric measurement of the ADR heat load on the He tank during Gross Cycle Control.

than making up for the difference. For simplicity, the calculations only use the latent heat of liquid helium at the tank temperature.

4.9. ADR Performance

The ADR hold time under Tight Temperature Control (TTC) was measured for two cycles when the He tank temperature was held at approximately 1.3 K. The hold times at 60 mK were 25.7 hours and 26.7 hours, respectively, exceeding the minimum required hold time of 20 hours.

The ADR heat load on the He tank was measured on the second Gross Cycle Control (GCC) and the third GCC. The heat load was measured calorimetrically by measuring the temperature change on the liquid helium in the He tank. Combined with a knowledge of the specific heat of liquid helium, the amount of liquid in the He tank and the total volume of the He tank, the heat dumped was 22.3 J on the second GCC and 22.5 J on the third GCC. This compares with 20.7 J measured for Astro-E XRS obtained during ground tests. The first GCC was not used in the analysis because it was done from a starting ADR temperature of ~ 1.3 K, which would result in a greater heat load to the bath and is not the normal mode of operation on orbit. The second and third GCCs took 64 minutes to completely execute (transition to TTC). The last part of the heating, as indicated in figure 11, is due entirely to magnet hysteresis. We find 4.5 J dumped in this part of the cycle alone. Since the hysteresis heating is symmetric, we expect a total magnet dissipation of 9.0 J per cycle. This compares with 6.4 J measured for the Astro-E XRS magnet. This alone more than covers the difference in heat dumped between the Astro-E and Astro-E2 XRS ADRs.

Combining the GCC time with the TTC duration and dividing the total into the average heat load gives an average power into the Cryostat from the ADR of 228 ± 5 μW.

On orbit the expected He tank temperature is 1.21 K. At this lower temperature the beginning current in the TTC and the parasitic heat into the ADR will both be much smaller. The estimated effect on hold time goes as $T^{-3.6}$ from measurements on Astro-E XRS. Using this extrapolation, it is estimate that the hold time on orbit will be 33.7 hours. The heat dumped per GCC and the duration of the GCC are expected to be approximately the same, so the average heat load to the He tank from the ADR on orbit will be 179 ± 20 μW. The larger error is due to the uncertainty in the extrapolation.

4.10. Expected On-orbit Lifetime

The thermal model used to predict lifetime shows that there is a "rebate" for heat added directly to the He tank in the form of reduced parasitic heat due to increased vapor cooling. It is therefore important to use the model to combine the measured parasitic heat into the He tank with the heat dissipated in the He tank by the ADR on a periodic basis. Note that while the ADR heat is dumped to the He tank over only 3–4% of the cycle, for the majority of the mission the large heat capacity of the helium and the low flow rate result in a very long time constant - on the order of two weeks. It is therefore allowable to use a constant extra heat from the ADR.

First the results for the benchmark boundary temperatures of 17 K at the Ne interface and 1.3 K at the He tank are calculated. To force the model to give the measured 903 μW instead of the 880 μW predicted, 35 μW is added directly to the He tank. Then the 228 μW from the ADR is added. The result is 1059 ± 41 μW. If we assume a 90% fill (out of a nominal 32.3 liter volume) at launch (the low temperature top-off rehearsal for Astro-E XRS resulted in 93%), then the heat load leads to a lifetime of 2.75 ± 0.11 years.

If we then use the expected boundary conditions of 16.24 K at the Ne tank, and 1.21 K at the He tank, the total heat load is calculated to be 952 ± 69 μW resulting in a lifetime of 3.01 ± 0.22 years starting from 90% full at launch. The 16.24 K value for the He tank is the highest of three temperatures measured on the engineering model (EM) Dewar Ne tank for Astro-E XRS. It is also conservative in that the EM Ne tank has a known higher heat load than the flight Ne tank, and that the heat load was higher due to 300 K ambient temperature on the outer shell rather than the < 280 K expected on orbit. The 1.21 K He tank temperature is derived from impedance measurements on the EM Dewar helium vent plumbing and the porous plug measurements made from XRS-2.

5. Ne Dewar

The Ne Dewar of the XRS is a vacuum-insulated vessel that provides a 17 K enclosure to the He Insert using solid neon and maintains the cryogenic environment during ground testing,

Table 4. Requirements for the Ne Dewar.

parasitic heat load to He tank*	$< 778\ \mu$W
neon temperature	< 17 K
neon lifetime	> 2 years (goal: > 3 years)
amount of solid neon	> 120 liters
main shell temperature	< 230 K

Notes.

* The total heat load to the He tank is composed of parasitic heat load from 17 K (778 μW), time-average ADR heat load (270 μW), heat input from FEA (JFETs; 95 μW), and thermal feedback from vapor cooling.

launch, and in orbit (Fujimoto et al. 2006). The ultimate design requirement (goal) for the Ne Dewar is to achieve a lifetime of 2 years (3 years) in orbit, under various constrains at launch and in orbit. In this section, we describe the design of the Ne Dewar and its performance.

5.1. *Requirements and design concept*

A preliminary design of the Ne Dewar was performed in 1994 (Volz et al. 1996). To keep ~ 30 liter (> 27.5 liter) superfluid liquid helium for more than 3 years, the total heat load to the He tank must be smaller than 1 mW (table 4). We adopted 120 liter solid neon as the second cryogen, which provides 17 K enclosure to the He Insert.

As with the He Cryostat, the design challenge of the Ne Dewar was to achieve 2–3 year lifetime of solid neon in orbit and to sustain against the mechanical environment during the launch. Since *Suzaku* is in a low-earth orbit, with the altitude of about 568 km, and performs pointing observations, there is a considerable heat input from the earth. Moreover, the vibration and the shock levels during the launch of M-V rocket are also very severe. The qualification test levels for the vibration in the axial and lateral directions are 5.4 $G_{\rm rms}$ and 6.8 $G_{\rm rms}$, respectively, while that of the shock is 15 $G_{0-{\rm p}}$. To mitigate the shock level on the Dewar, the Ne Dewar mounting has shock absorbers and support straps optimized to satisfy these conflicting requirements.

5.2. *Design of the Ne Dewar*

Figure 12 and 13 show a side view and a cross section of the Ne Dewar, respectively, while figure 14 shows a schematic view of the plumbing. As shown in these figures, the Ne Dewar is composed of a 120 liter toroidal tank, a main shell, three vapor-cooled shields (VCS), multi-layer insulators (MLI), plumbings to the He and Ne tanks, valves, aperture for x-rays, and mechanical structures to support these components, i.e., support straps and shock absorbers. For the Dewar of the Astro-E2 XRS, a single-stage Stirling-cycle mechanical cooler is installed at the Dewar girth ring, which is described in section 5.3. The total dry weight of the Dewar

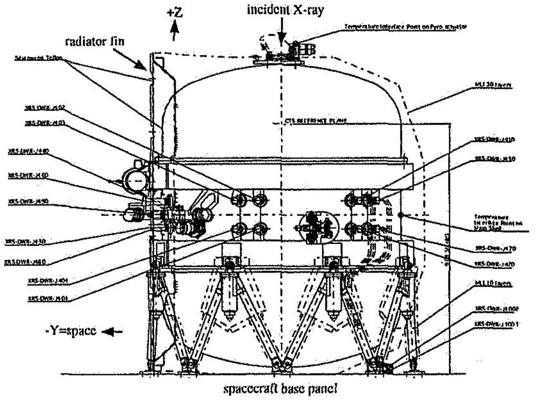

Fig. 12. Side view of the Ne Dewar.

including the He Insert and the mechanical cooler is 223.26 kg, and design values of the initial mass of the solid neon and liquid helium are 172.8 kg and about 4.3 kg, respectively, bringing the total weight at launch to 400 kg.

The Ne tank is machined from aluminum alloy as two shells with 2 mm wall thickness. The shells are then filled with an aluminum foam and joined. The foam works as a heat exchanger and keeps the neon temperature uniform. At the inner surface of the toroidal tank, there is an interface flange, called 17 K interface, four attaching the He Insert. The top and bottom ends of the Ne tank are closed out with shrouds connected to the Ne tank. Once the tank is filled with solid neon, all of the Ne tank valves are closed until launch. On the ground, it is regularly cooled down by flowing liquid helium around the Ne tank through V5 shown in figure 14, so that the neon temperature is kept below its melting point (24 K). Soon after the launch, the Ne vent valve (V9) is opened, and pumping down starts. This keeps the neon temperature below 17 K.

The Ne tank is supported by 12 straps connected to the main shell (figure 13). A significant fraction (30–40%) of the incoming heat to the Ne tank is from thermal conduction through these support straps. Therefore, it is crucial to make the thermal conductance of the straps as small as possible, while keeping the strength to withstand the mechanical environment at launch. To meet these requirements, we adopted S2-GFRP (glass fiber reinforced plastic) belts as straps and titanium alloy as joints. We also introduced shock absorbers using belleville springs at the joints of the main shell and the support legs. These mitigate shock to the Ne tank during launch by about 20%. As a result, straps with a cross section of 16.6 mm $\times$ 1 mm were

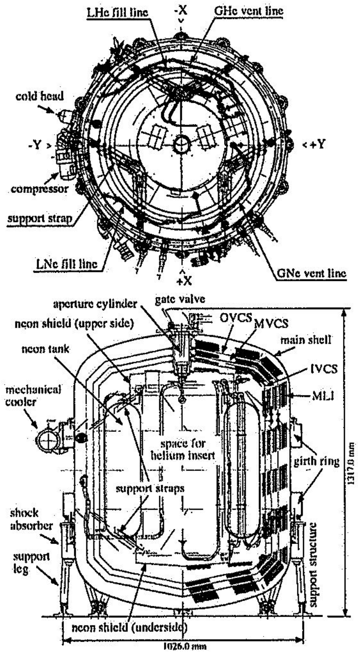

Fig. 13. Cross section of the Ne Dewar. The radiator fin is not shown in this drawing.

adopted, which is fatigue limited, and the fraction of the heat load to the Ne tank attributed to the support straps was reduced to about 25% (see also figure 36 in section 10.1).

Thermal insulation is achieved by the main shell, VCS, and MLI. The main shell is the outermost container made of 3.0–3.5 mm thick aluminum alloy. Its height and diameter are 1184.5 mm and 926 mm, respectively. Part of the main shell surface is exposed to space, and works as a radiator. This area is coated with silver Teflon tape. The unexposed part of the Dewar surface, which is interior to the spacecraft, is covered with MLI, 10 layers around the support structure and 30 layers for other part. A radiator fin is attached to the main shell, which fills the gap between the Dewar and the spacecraft (figure 12). Using these radiators, the main shell surface temperature is kept at about 230 K when the mechanical cooler is off, and at 250 K when the mechanical cooler is operating with full power. Between the main shell and

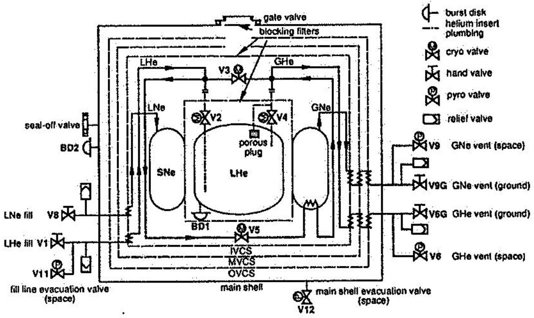

Fig. 14. Schematic view of the plumbings and valves inside the Ne Dewar.

the Ne tank, there are three vapor-cooled shields, inner (IVCS), middle (MVCS), and outer (OVCS), which are cooled by sublimed neon and evaporated helium. These shields are made of 0.4 mm thick aluminum alloy. There are multi-layer insulators (MLI) between the main shell and the OVCS (50 layers), OVCS and MVCS (30 layers), MVCS and IVCS (20 layers), and IVCS and the Ne tank (20 layers). The VCS's and MLI reduce incident radiation from the main shell to the Ne tank.

In addition to the manual and electromotive cryo-valves for ground operations, there are five pyro valves, for venting helium (V6), venting neon (V9), evacuating helium fill-line (V11), evacuating guard vacuum (V12), and for the x-ray aperture (gate valve). All these valves are opened with pyro cutters after launch. At the center of the gate valve of the Astro-E2 XRS, there is a beryllium window with 100 μm thickness and 5 mm radius. This allows performance verification of the detector on the ground and during initial phase in orbit using an ^{55}Fe radioisotope source, without opening the gate valve.

There are 7 flight and 7 GSE temperature sensors in the Dewar[2], three ruthenium-oxide sensors for the Ne tank, and one platinum sensor for IVCS, MVCS, OVCS, and the main shell, respectively. These sensors are activated and measured by ACHE. Manganin twisted pair cables were used for the temperature sensors and the electromotive cryo-valves in the Dewar. Custom-made flat cables are used for the calorimeter sensor channels and some temperature sensors inside the He Insert. The magnet lead is a twisted pair made of oxygen-free copper, and is laid down inside the plumbing for venting neon gas.

In this design (without a mechanical cooler), the total heat input to the Ne tank was 295 mW, and the expected lifetime of the solid neon was estimated to be 1.95 years. This

---

[2] This number does not include the sensors inside the He Insert and for the x-ray filters.

Table 5. Specifications of the mechanical cooler adopted for the *Astro-E2* XRS Dewar.

cooling power	2.4 W/100 K (BOL), 2.0 W/100 K (EOL)
power consumption	0–35 W
drive frequency	52 ± 1 Hz with 0.1 Hz step
life time	> 3 years
weight	4.2 kg (cold head + compressor)

is slightly shorter than the requirement (2 years), although it is very close. For Astro-E, we fabricated two Dewars, an engineering model (EM) and a flight model (FM), and verified the thermal performance. The measured heat load from the Ne tank to the He tank was 629 μW (without the ADR heat loading), which was well below the requirement. Hence, the lifetime of the Astro-E XRS in orbit would have been limited by the amount of solid neon to 1.95 years.

5.3. Mechanical cooler

One of the major design changes from Astro-E to Astro-E2 was that the adoption of a mechanical cooler. Since the lifetime of the Astro-E XRS was slightly shorter than the requirement, we extensively investigated a possibility to extend the lifetime of solid neon with minimum risks when we started Astro-E2 in 2000. A solution that we found was to cool down the OVCS with a mechanical cooler from 195 K (Astro-E) to 135–100 K, depending on 50–100% operation duty. Then the expected lifetime would be increased to 2.4–3.5 years. More importantly, a lifetime of 1.92 years can be achieved even if the mechanical cooler fails or is otherwise not operated in orbit. Microphonics was a concern from the viewpoint of the detector performance. However, since the visibility of *Suzaku* is typically 40–50% due to earth occultation and SAA (South Atlantic Anomaly), we had the option to reduce the power or not to operate during the observation. Therefore, we concluded that there was virtually no risk to installing the mechanical cooler for the Astro-E2 XRS Dewar.

The mechanical cooler adopted for Astro-E2 is a single-stage Stirling-cycle cooler developed by SHI (Narasaki et al. 2006). Both the cold head and the compressor are mounted on the surface of the Dewar girth ring (see figure 12 and 13). The compressor is in face-face-type configuration, and by adjusting the mass balance, vibrations can be significantly reduced. The mechanical cooler is driven by XRS-CDE (Cooler Drive Electronics), with a commanded voltage. Drive frequency is 52 ± 1 Hz, and is adjustable with 0.1 Hz step. The maximum power of the cooler is 35 W, with an initial cooling power of 2.4 W at 100 K. The drive circuit is grounded at the CDE. The vibration level at the girth ring due to the mechanical cooler was about 10 mGrms. Its impact to the detector performance was measured after the Dewar fabrication completed, and is described in section 9.5.

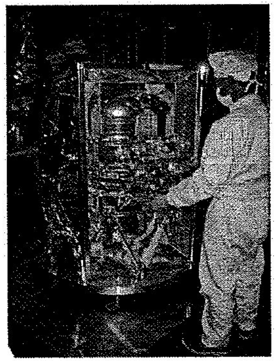

Fig. 15. Finished XRS Dewar prior to spacecraft iteration. The rectangular frame attached to the Dewar is the thermal close out panel (radiator fin) that mates to the spacecraft. The mechanical cooler cold head and compressor are mounted to the upper girth ring.

5.4. Fabrication and ground operations

Fabrication of the Ne Dewar for Astro-E2 XRS started at SHI in 2001. The He Insert, assembled at GSFC, was integrated into the Dewar in 2004 March, and assemble of the Dewar completed in 2004 June. After one month of the main shell evacuation, and three weeks of performance verification tests of the cryogenic system and the detector at SHI with about 10% of solid neon in the Ne tank, the Dewar was carried to ISAS/JAXA. In 2004 September, the Ne tank was filled with liquid neon, which was frozen by flowing liquid helium around the Ne tank, and the Ne valves were closed. Total mass of the solid neon filled in the tank was 173.24 kg. Then the Dewar was mounted on the spacecraft.

During the ground test phase of the spacecraft, solid neon was cooled down approximately once per three weeks, and was kept at 13–21 K. In addition, to ensure that water vapor from outgassing MLI remained intact after being adsorbed during cold down, the IVCS was maintained below 140 K using a liquid level detector as a heater and evaporating liquid helium to produce vapor cooling of the IVCS. This operation was repeated almost everyday until launch.

6. Dewar Aperture and Blocking Filters

The Aperture Assembly supports four of the filter mounts, the DMS, IVCS, Ne, and FEA and their associated filters. There are three sub-assemblies: the aperture cylinder, the neon filter mount, and the FEA filter mount. The assembly is designed to support the filters

Table 6. Properties of the blocking filters[*THESE ARE XRS1 NUMBERS AS PLACEHOLDERS*]

		Nominal Thickness			Temperature
Serial Number	Pinhole Trans	Polyimide	Aluminum	Mesh	(K)
CTS-FM-05	3.80×10^{-4}	737 Å	508 Å	None	0.060
FEA-FM-201	4.33×10^{-4}	737 Å	508 Å	None	1.3
Neon-FM-202	3.59×10^{-8}	1023 Å	1088 Å	None	17
IVCS-FM-204	2.69×10^{-8}	1025 Å	1088 Å	None	120
DMS-FM-201	1.31×10^{-5}	1060 Å	802 Å	70 lines/inch Ni (T=78 %)	250

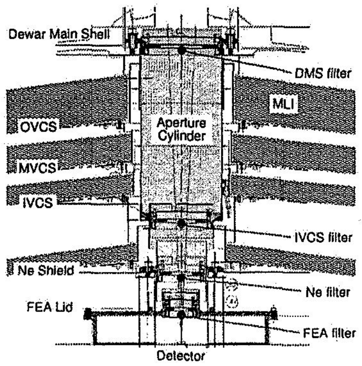

Fig. 16. Cross section of the aperture assembly.

within the optical path at the following design temperatures DMS (230–240 K), IVCS (86–126 K), Neon (17 K) and FEA (1.3 K). A secondary requirement of the filter mounts is to prevent the the flow of water vapor onto the (cold) filter membranes via a nested set of baffles. The Aperture Cylinder, which holds the DMS filter at one end and the IVCS filter mount at the other, is attached at the Dewar at the main shell. The IVCS end of the cylinder is cantilevered with a thermal strap connecting it to the IVCS shield. The Neon Filter Mount is attached to the top of the Dewars Neon shield and the FEA Filter is mounted in a custom FEA Lid/Filter Mount (see figure 16).

7. Filter Wheel

The XRS Filter Wheel (FW) is designed to reduce the counting rate on XRS and provide x-ray fluorescence lines for in-flight calibration. It consists of the filter wheel unit and an electronics called the Filter-wheel Driving Electronics (FDE). The assembly of the FW was

`filter_transmission.eps`

Fig. 17. The x-ray transmission of all five optical blocking filters (black) and the HgTe absorber quantum efficiency (grey). The discrete absorption edges are labeled.

carried out by NEC Toshiba Space Systems, Ltd. Original design for Astro-E was presented by Furusho et al. (1999) and several improvements were implemented for *Suzaku*. The wheel has 6 mounting spaces for filter elements and the center is directly connected to the shaft of a MOOG's stepper motor (see figure 18). The filter disk has a circular slit wall running along the outer edge and position sensors consisting of three pairs of a photo-diode (PD) and an LED measure the three slit positions. The housing of the filter is 186 mm in diameter and mounted on the middle deck of the spacecraft. The total weight of filter wheel unit is 850 ± 0.1 g. The distance between the XRS detector plane and the filter elements is 397.5 mm, where x-ray image from the XRT has a diameter of 39.2 mm. The diameter of the filter elements is 49 mm, and effective opening diameter is 44 mm. The filter elements are summarized in table 7. Neutral Density (ND) filters of 10% transmission are made from 200 μm thickness Mo plate with 1802 pin holes. X-ray transmission was measured by raster-scans of 1.4 mm × 0.45 mm x-ray beams. Using Al Kα (1.487 keV), Ti Kα (4.509 keV) and Cu Kα (8.041 keV) lines, the transmission is consistent with $9.53 \pm 0.15\%$. The low-energy cut filters are Be plates of 300 μm thickness. The x-ray transmission were measured at 5 different energies (1.776, 2.294, 4.509, 8.041, and 8.400 keV) and fitted well by a 272.2 ± 0.2 μm and 267.7 ± 0.2 μm Be with contaminations dominated by a $0.03 \pm 0.02\%$ Fe. Gradation of thickness caused by rolling process were found at 6% at most and would be incorporated into the XRS response functions.

Calibration sources of ^{55}Fe (Kα_1: 5.899 keV, Kα_2: 5.888 keV, Kβ: 6.490 keV, $T_{1/2} =$ 2.73 yr) and ^{41}Ca (Kα_1: 3.314 keV, Kα_2: 3.311 keV, Kβ: 3.590 keV, $T_{1/2} = 1.03 \times 10^5$ yr) are introduced to *Suzaku* and are mounted at the position 2, 4 and 6 as shown in table 7 and figure 19. Those sources are carefully designed to survive the vibration during the launch. The ^{55}Fe sources are electro-deposited on copper blocks and are coated by a thin Ni. The ^{41}Ca source is packed in a screw-like SUS holder shielded by a 50 μm Be window. Estimated counting rate on a XRS pixel at the launch are $\sim 0.145\ \mathrm{c\,s^{-1}\,pixel^{-1}}$ for ^{55}Fe and $(9.2\pm0.6)\times10^{-4}\ \mathrm{c\,s^{-1}\,pixel^{-1}}$ for ^{41}Ca in vacuum. On the ground calibration test, ^{55}Fe were irradiated through the gate valve and counting rates were consistent with the estimation.

The FDE control the filter wheel operation based on commands and process position data. The main part of the electronics which controls the stepper motor consists of an HIC (Hybrid Integrated Circuit) which generate three phase control signals. By command, the FDE can rotate the filter wheel with 1 step, 20 steps (1°), and 1200 steps (60°) in a specified clockwise/counterclockwise direction. The position of the filter wheel is monitored and checked by three difference methods, as the number of step signals from the HIC, the number of an optical encoder counter mounted within the motor, and the signal pattern of LED/PD pairs through the slits at the filter-wheel edge.

The FW was switched off at position 1 (fully open) before the launch and powered on 2005 July 24, 14 days after the launch. The basic functions were tested and ^{55}Fe source was irradiated on the XRS through the gate valve on 2005 August 3. Unfortunately, the filters were not used for observation. Endurance test for the stepper motor continues once a day with ±60° rotation, and no damage is observed at present.

Table 7. Properties of Filters & Calibration Sources

Position	1	2	3	4	5	6
Filter	open	open	Be 300μm	Be 300μm	ND 10%	ND 10%
Cal. Source	-	^{55}Fe,^{41}Ca	-	^{55}Fe	-	^{55}Fe
Material	-	-	Be	Be	Mo	Mo
Hole Diameter*	-	-	-	-	320(2)μm	320(2)μm
Weight*	-	-	1.006(1) g	0.988(1) g	3.565 g	3.565 g
Thickness†*	-	-	288.7(9) μm	283.5(9) μm	200 μm	200 μm
Transmission‡*	-	-	-	-	9.53(2) %	9.53(2)%

Notes.

* Numbers in parentheses denote errors in measurements.

† Thickness of Be filters are calculated from the weight.

‡ Transmission of ND filters are average of x-ray transmission measurements.

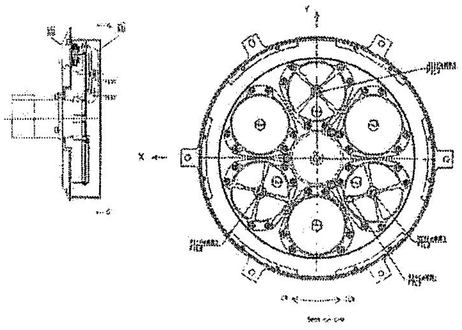

Fig. 18. Design of FW. Left: Side view in the housing, Right: Bottom view without housing.

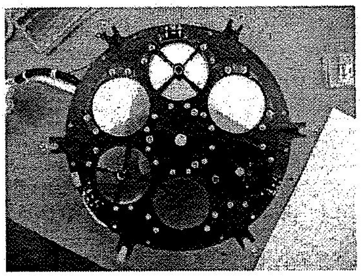

Fig. 19. Photograph of filter elements and dummy calibration sources installed on the FW disk.

8. Instrument Electronics

8.1. *Analog Electronics*

The Calorimeter Analog Processor (CAP; see figure 20) provides power and bias to the detectors and first-stage JFETs, amplifies the detector signals, and controls the temperature of the first-stage JFETs. The CAP consists of two identical A and B sides, each of which handles 16 channels.

The cold JFETs located in the FEA convert the $\sim 30\ \mathrm{M\Omega}$ detector impedance to about $2\ \mathrm{k\Omega}$ for transmission to the CAP. Their operating temperature of 130 K is controlled by the CAP.

There are 4 detector bias supplies, each of which supplies the bias voltage to 8 detectors.

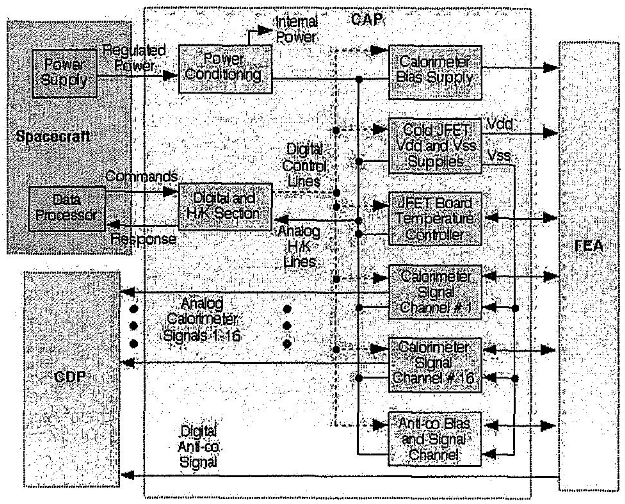

Fig. 20. Block diagram of the Calorimeter Analog Processor (CAP).

Likewise, there are 4 V_{dd} supplies, each supplying power to 8 of the cold JFETs.

The CAP contains 32 amplifier circuits, one for each detector pixel. Each amplifier is implemented in a hybrid circuit package. The amplifiers have an AC gain of 20,000 and a highpass knee of 10 Hz. Their output is a full differential signal (maximum 24 V), which is sent to the Calorimeter Digital Processor (CDP). The temperature stability of the amplifiers is better than 200 ppm/°C. The signals are AC coupled, with a single pole at 10 Hz.

8.2. *Digital Electronics*

The signals from the CAP (Stahle et al. 1999) are voltage pulses, with a maximum amplitude of 24 V, as shown in figure 21. The voltage at the detector actually decreases during a pulse, but the differential output of the CAP is reversed for convenience, giving a positive-going pulse at the input to the CDP.

Due to telemetry limitations, pulses must be detected and processed on-board. This is the job of the Calorimeter Digital Processor (CDP). The CDP is configured as 32 independent channels, one per pixel, all running the same software. It also contains common circuitry to handle communication with the spacecraft. Figure 22 shows a block diagram of the CDP.

Each channel contains an attenuator, antialias (AA) filter, 14-bit Analog-to-Digital Converter (ADC) running at 12288 Hz, a microprocessor with 64 KBytes of Static RAM, and interfaces to the rest of the system.

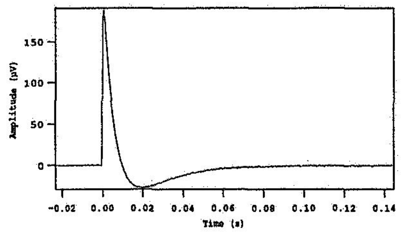

Fig. 21. A typical pulse from one detector. The x-ray raises the temperature of the thermistor, thus lowering its resistance. This causes a drop in the voltage across it. For convenience, the pulse is inverted by the CDP. The pulse overshoots its baseline because of the AC coupling in the CAP.

Each channel in the CDP is responsible for a single pixel in the detector array. The CDP processing detects pulses, processes them, and sends the data to the spacecraft. Each x-ray pulse detected results in a 64-bit data packet, containing the pulseheight, the risetime of the pulse, a measure of the pulse shape, a time tag with 5 μs resolution, the pixel number, and 6 one-bit flags. The flags indicate event grade, whether the anticoincidence detector fired, whether the pulse was electrically clipped at the ADC, and whether it is a "baseline" pulse. Baseline pulseheights are created by processing a noise record as if it were a pulse, and are used to obtain a measure of the noise in the system.

8.3. *Pulse Detection*

The first job of the DSP is to detect pulses in the data stream. Detecting initial pulses is easy; the hard part is finding small secondary pulses on top of large ones. The reason is shown in figure 23, which is a simulation of a 200 eV secondary pulse 2 milliseconds after a 10 keV initial pulse.

Clearly, the secondary pulse is not detectable with a simple level discriminator, or even a simple discriminator based on the signal derivative (since the derivative never goes positive for the secondary pulse). However, the pulse detection algorithm does start with a smoothed derivative of the data. The derivative is calculated by convolving the data with a "boxcar derivative" function, as shown in part (A) of figure 24. The number of samples (the length of the boxcar) is an adjustable parameter.

The initial pulse is detected using a simple level discriminator on the derivative. The threshold is set as low as possible given the noise level in the system.

In order to detect secondary pulses, the CDP maintains a copy of the single-pulse deriva-

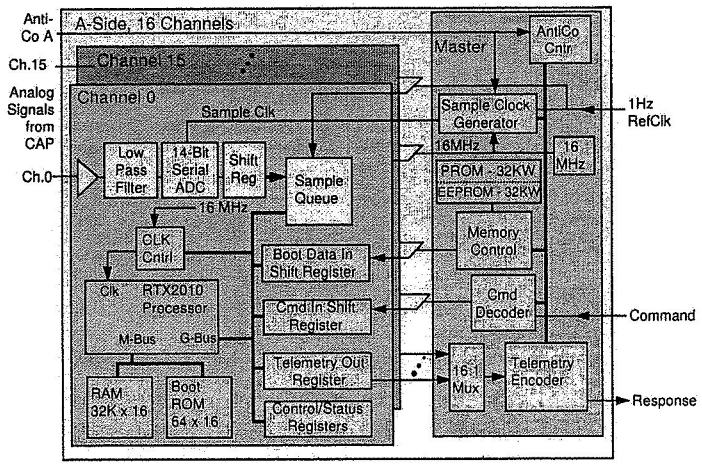

Fig. 22. CDP block diagram. There are 2 completely independent "sides", labeled A and B, for redundancy. Each side comprises a "master" circuit which handles commands and telemetry and stores the DSP code in PROM and EEPROM, and 16 DSP channels. One channel is shown in the diagram.

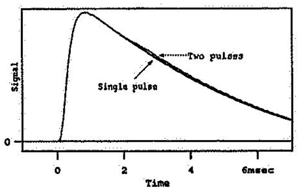

Fig. 23. A 200 eV pulse 2 ms after a 10 keV initial pulse.

tive shape. When an initial pulse is detected, this derivative shape is scaled by the pulse amplitude and subtracted from the calculated derivative to form an adjusted derivative.

A secondary pulse is provisionally triggered when the adjusted derivative exceeds a discriminator threshold. In normal operation this threshold is set to the same level as the initial pulse threshold. The provisional trigger becomes an actual secondary pulse detection only if the adjusted derivative peaks and returns to zero within a specified length of time.

Upon detection of a secondary pulse, the single-pulse derivative shape is appropriately

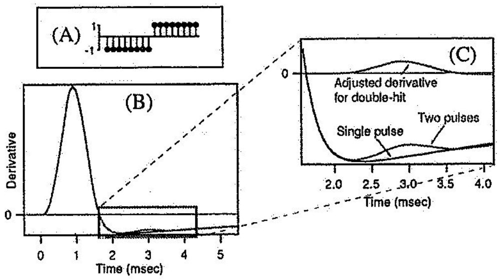

Fig. 24. (A) The form of the boxcar derivative. (B) The derivative of a single pulse, and of the double pulse from figure 23. (C) Magnified view of the derivatives where the second pulse occurs, including the *adjusted derivative*, which is the difference between the single pulse and double pulse derivatives.

scaled and offset, then added to the original correction curve used to calculate the adjusted derivative.

8.4. Pulseheight Analysis

The CDP calculates the height of each pulse by using an optimal filter, which is a matched filter that has been weighted in frequency space by the noise in the system. The details of this calculation are given in Boyce et al. (1999).

The length of the optimal filter is 2048 samples, which corresponds to 166 ms. For pulses separated by this much time, the full optimal filter is applied, giving what is known as a "hi-res" pulse. If two pulses are closer than 2048 samples, but more than 512 samples, a quarter-length optimal template is used, yielding a "mid-res" PHA. If they are closer than that, a simple measure of the peak pulseheight is used, giving a "low-res" event. Low-res events are significantly lower resolution than hi-res, having a $\Delta E/E$ approximately 5 times worse. The events in the data stream are tagged with the event grade.

In the absence of noise tones (noise at a single frequency), the mid-res pulses have approximately the same resolution as the the hi-res ones. If there are noise tones, then mid-res pulses will have lower resolution than hi-res. We typically saw many noise tones during instrument testing on the ground (mostly power-line harmonics and computer vertical sweep harmonics). Once the instrument was integrated onto the spacecraft, the noise became essentially flat with frequency.

The CDP also tags events with a "secondary" flag, which indicates that an event fell on the tail of a previous event. So if a pair of pulses arrives 10 ms apart, they will both be low-res,

Table 8. Event grades as a function of time since previous pulse (t_1) and time until next pulse (t_2). H:Hi-res, M:Mid-res, L:Low-res, S:Secondary. Times are in milliseconds.

	$t_1 < 35.5$	$35.5 < t_1 < 142$	$t_1 > 142$
$t_2 < 35.5$	LS	LS	L
$35.5 < t_2 < 142$	LS	MS	M
$t_2 > 142$	LS	MS	H

but only the second one will be marked secondary. Secondary events suffer from reduced gain, since the detector is still warm (and hence less responsive) from the first event. It is possible to account for most of this gain error by applying an exponential correction to the secondary pulseheight, based on the size of and time since the preceding pulse. All events are time-tagged, which allows us to correct fairly effectively for the reduced gain of secondary events.

It is important to note that each individual event is analyzed with the best possible resolution; there are no resolution modes. In fact, once collecting science data, the CDP has no modes at all.

Table 8 indicates the grade for an event separated in time from a preceding event by t_1 ms and from a subsequent event by t_2 ms, all three events occurring on the same pixel. This assumes that the mid-res template is 1/4 the length of the hi-res template, which is the usual case.

The fraction of events in each grade can be calculated easily, assuming a Poisson distribution of photons, using the information in table 8. The results are shown in figure 25. Figure 25 also shows an estimate of the fraction of events which are missed entirely, because they are too close to the preceding pulse. If two pulses are too close to be detected individually (about 0.7 ms apart), they will be measured as a single event, with a pulseheight approximately equal to the sum of the two individual pulseheights. Such events also have a very broad range of risetimes, since even a small offset in time leads to a noticeable S-shape in the rise of the combined pulse.

Along with pulseheight, time, and flags, each event includes a measurement of the pulse risetime. this is useful to identify certain classes of "bad" events.

We determine the risetime by fitting a straight line to a fixed number of points centered at the 50% amplitude point of the rise. Normally we use 3 samples, but this can be changed by a command. We use a fixed number of points to eliminate a source of bias in calculating the risetime. If we use all the points from, say, 10% to 90%, then there are discrete jumps in risetime between pulses with N points on the rise and pulses with $N + 1$ points. This is because the rise is S-shaped, and so adding one more point to the calculation always increases the risetime.

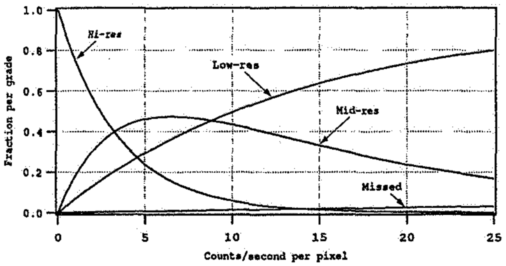

Fig. 25. The fraction of events which fall into each grade, as a function of count rate per pixel. This applies to each pixel individually.

Table 9. Mass and nominal power of the electronics boxes.

	mass* [kg]	nominal power [W]
CAP	4.95	7.8
CDP	5.89	12.0–13.4
ACHE	9.10	22.0 (43.3†)

Notes.

* Does not include shorting plugs and EMI filters.

† When the ADR magnet is fully charged.

In order to avoid contaminating the data with particle hits, we have an anticoincidence detector (Stahle et al. 1999). The antico detector is a silicon PIN diode just under the pixel array. When it is triggered, the CDP receives a pulse. If an antico pulse occurs anytime within an adjustable window near the beginning of a detected x-ray pulse, that event is tagged with the Antico flag.

9. Pre-launch Tests and Calibration

The XRS underwent extensive component-level testing while at NASA/GSFC during the winter of 2004 (Cottam et al. 2004). Testing at the full instrument level took place at SHI in the summer of 2004, prior to the final integration onto the spacecraft At ISAS in September 2004 (Cottam et al. 2006). Then, a series of spacecraft functional and environmental tests were performed until 2005 April at ISAS/JAXA (Ota et al. 2006). We characterized the spectral performance of the XRS by the energy scale, the line spread function, the instrument background and the necessary elements to obtain the effective area. In the following sections we will present the main results of our instrument characterization and ground calibration.

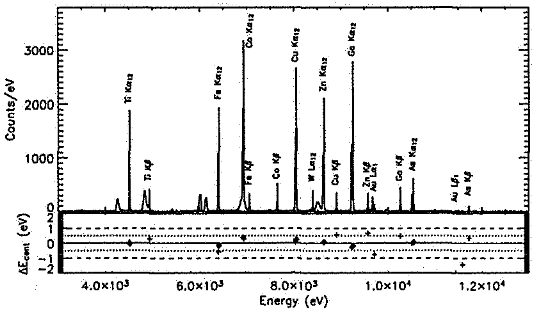

Fig. 26. An energy-corrected spectrum obtained during ground calibration and the residuals between the measured and laboratory energies for the brightest lines. The diamonds represent the Kα lines that were used to generate the energy scale.

9.1. Energy Scale

The XRS energy scale, which maps the measured pulse heights to the energy of the incident photons, is a complex, non-linear function that depends not only on the design parameters of the XRS array and the pulse detection algorithm, but also on the operating conditions, including the thermal environment seen by the array and even the photon flux. Because of the inherent complexity, the energy scale is currently determined by empirically fitting measured pulse heights from known energy sources to a third-order polynomial function.

During ground calibration, the energy scale is determined by illuminating the array with fluorescent emission lines. We were able to generate energy scales that are accurate to better than $\Delta E_{\mathrm{centroid}} \sim 1.0$ eV (figure 26). Because the energy scale depends on the specific operating conditions, a new energy scale will be generated in-flight using both onboard radioactive sources and astrophysical sources. We have performed extensive ground calibration of the XRS energy scale to parameterize the effects that changes in the thermal conditions in-flight will have on the energy scale. The calibration pixel, and the thermal history of the instrument will be used to track these changes.

9.2. Line Spread Function

The XRS Line Spread Function (LSF) consists of a Gaussian resolution kernel and a low energy tail. The resolution kernel is primarily determined by phonon and Johnson noise. These produce a Gaussian distribution in the measured energy around the nominal value. In addition to the Gaussian core, the XRS LSF contains a low-energy shoulder that is caused by photo- and electron escape events.

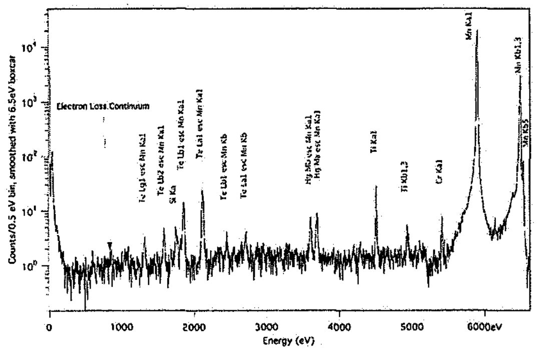

Fig. 27. The broadband XRS response to the ^{55}Fe source. The low energy redistribution tail includes fluorescent escape line from the Hg and Te in the pixel absorbers.

The LSF has been measured by illuminating the array with a ^{55}Fe electron capture source and several characteristic fluorescent emission lines. Figure 27 shows the measured XRS response to the Mn Kα line from the ^{55}Fe source. Except at low energies where the electron loss continuum begins to contribute, the XRS resolution kernel can be successfully described by a single Gaussian. The composite resolution for the array, excluding two outlying pixels is ΔE(FWHM) < 6 eV at 6 keV. The energy resolution is only weakly energy dependent, increasing from ~ 6 eV at 5.9 keV to ~ 7.5 eV at 9.3 keV. The energy resolution is not expected to change significantly in-flight.

9.3. Effective Area

The effective area of the XRS includes the effective area of the telescopes, the overlap fraction between the mirror PSF and the detector pixel absorbers, the transmission of the five optical blocking filters, the detector quantum efficiency, and electronic deadtimes. The full XRS effective area, based on everything measured prior to launch is shown in [i]figure 2 in section 1. The discrete structure in the effective area curve is dominated by the quantum efficiency of the HgTe absorbers at high energies and the transmission of the blocking filters at the low energies, both of which have been characterized extensively on the ground.

9.4. Pulse Height-Energy Gain Determination

To attain the best energy resolution of the XRS, correction of temporal gain changes is mandatory since even a 0.1% gain change corresponds to an energy shift of 6 eV for a 6 keV photon and can significantly degrade the energy resolution. In figure 28a, an example of the gain drift curve is shown. The energy shift of the order of 10 eV for the Mn Kα line was observed during a 24-hours running test.

The simplest way to correct the gain drift is to monitor the Mn Kα line energy with the calibration pixel and apply its gain correction factor to the thirty active pixels (method 1). The gain correction factor, $f_{\rm drift}$, was derived by calculating a ratio between the observed mean energy channel and the mean Mn Kα energy of 5894.397 eV (a weighted mean energy of the eight Lorentzian line components; ref) every 100 events. This method is effective when the gain variation is due to changes in the $\sim$ 60-mK heat sink temperature. However, different behavior among the pixels was observed; the inner 15 pixels show the smallest changes and the outer 15 pixels show more, and the calibration pixel shows the largest shift in energy (figure 28b). The corrections using method 1 resulted in the resolutions of $\sim$ 6–8 eV. As shown in section 3.2, we think that the temperature variations of the Ne and He baths cause small changes in a stray power seen by the array and affect the pixels differently depending on their positions.

^{55}Fe and ^{41}Ca sources are attached to the filter wheel and can be taken in the field of view of the array (see section 7), so we next performed the correction for each pixel by monitoring the Mn Kα line from the filter-wheel source (method 2; figure 28b). This self-calibration significantly improved the resolutions: the fitting of the composite XRS spectrum yields a FWHM of 5.73 ± 0.03 eV (figure 30) and most of the pixels have a FWHM of 5–6 eV.

The differences in behavior with temperature variation makes the drift correction algorithm complex. Although self-calibration (method 2) is very effective, use of the filter-wheel source will increase the background intensity which might compromise observations of faint objects. The gross cycle control (GCC) of the ADR is considered to be the dominant influence on the He and Ne temperature variations. We found through the ground tests that the gain is more unstable for the first 2–3 hours after a GCC (see figure 28). Thus periodic GCC operation may allow the gain-drift repeatability to correct the gain drift. The house-keeping data will be also useful to correct the differential gain drift between the calibration pixel and the main array. The ground experiments were thought to be out of equilibrium and the gain was likely to be more stable in orbit.

9.5. *Effect of the mechanical cooler*

Microphonic noise from the mechanical cooler (see section 5.3) was one of our concerns, and its impact was measured in two configurations, during the subsystem-level performance verification test at SHI in 2004 July–August with 10% solid neon, and during the spacecraft test phase with 100% solid neon.

In the fully integrated configuration on the spacecraft, noise spectra of the detector channels were very clean, when the mechanical cooler was off. Its level was 13–14 nV Hz$^{-1/2}$ up to 1 kHz, and there were no line components (figure 31a). When the mechanical cooler was operated with full power, there were several line components of 10th or higher harmonics in the noise spectra (figure 31a). Since the frequency range was high ($\gtrsim$ 500 Hz), however, it did not affect the energy resolution at all, and the instrumental width of 5.73 ± 0.03 eV (figure 30) was unchanged from that obtained while the cooler was off, within the statistical errors. A comparison of the instrumental width for each pixel is also shown in figure 32.

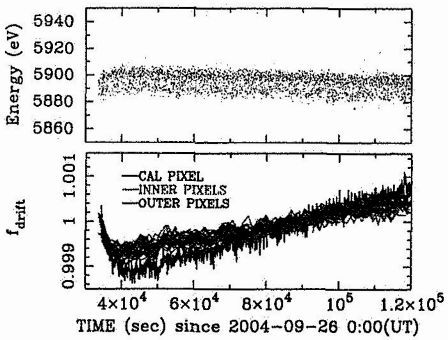

Fig. 28. Example of XRS pixel gain drift (a) and drift correction factor, $f_{\rm drift}$ for the calibration pixel, inner 15 pixels, and outer 15 pixels of the array (b). In panel (b) $f_{\rm drift}$ was derived every 100 events from the FW source (method 2). A GCC was carried out at 23:17 on 2004 September 25 (UT).

On the other hand, during the subsystem-level test with 10% neon, there were fundamental and harmonics line components in the low frequency range of the noise spectra, and the energy resolution became 6–8 eV (FWHM). However, the test configuration was quite different from that on the spacecraft, i.e., (1) the Dewar was set on a dolly and not firmly integrated to the spacecraft, and (2) long GSE harnesses were used instead of the flight harnesses. Therefore, we could not pinpoint the cause of the degradation.

As a conclusion, the mechanical cooler does not degrade the detector performance, at least in the initial phase when the amount of neon is $\sim$ 100%. In fact, this was verified using the inflight data. At the end of the mission, its impact is not large, and the energy resolution of 6–8 eV (FWHM) could have been achieved even in the worst case.

10. In-flight Performance of the XRS

10.1. *Dewar System*

Before the detector could eventually be cooled to its operational temperature of 60 mK, a number of critical steps were required to establish the proper thermal conditions. The Dewar He vent valve was successfully opened 235 s after launch in order to begin pumping the He bath while there was still a positive force due to acceleration on the He. This was required in

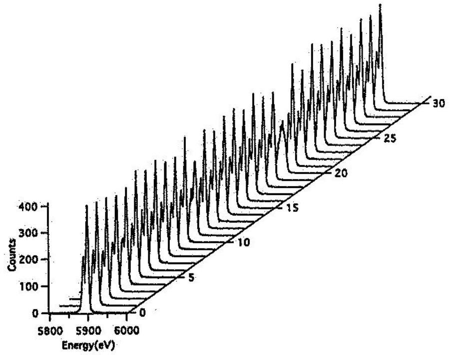

Fig. 29. Pulse-height histograms obtained using ^{55}Fe during spacecraft ground tests.

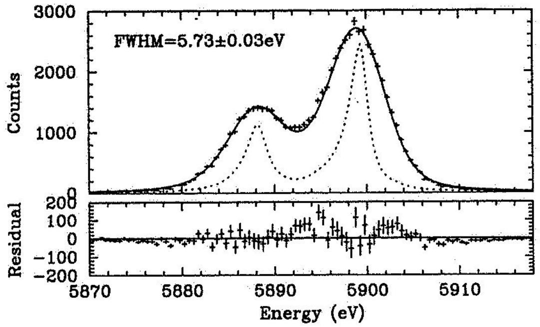

Fig. 30. Composite spectrum of Mn Kα_1 and Kα_2 for all XRS pixels except for the calibration pixel, 11 and 20, fitted to the intrinsic line shape (dashed curve) of Mn lines produced by an ^{55}Fe source. The solid curve is the best-fit to this profile assuming a Gaussian energy resolution kernel. The data were taken on 2004 September 28 at ISAS/JAXA, with the mechanical cooler running.

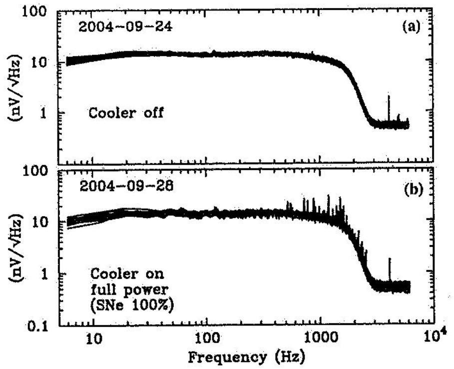

Fig. 31. Noise spectra of XRS pixels with the mechanical cooler off (a) and on at nominal full power and 52 Hz during the 2004 September functional test (b).

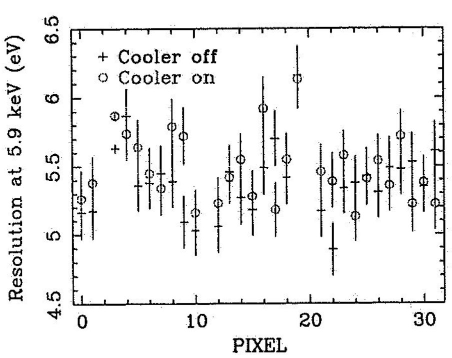

Fig. 32. Comparison of pixel resolution between the cooler-off and cooler-on data. The pixels 11 and 20 are outside the graph.

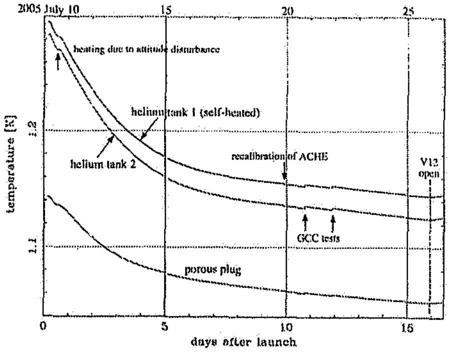

Fig. 33. Temperature history of the He tank (sensor 1 and 2), and the porous plug, from launch to the loss of helium.

order to establish the proper temperature gradient of the porous plug. The Ne vent valve and the He fill valve (down to the internal cryostat valve, which was closed prior to launch) were opened at about 27 minutes into the flight. The ACHE electronics were powered up 24 minutes after launch and temperature data were transmitted to the ground station at Uchinoura after the first earth orbit. The data confirmed that all of the temperatures sensors were reading nominally, indicating that the Dewar system had survived launch and that the porous plug had the proper temperature profile. With the He vent line open, the He temperature began to drop as expected. In figure 33 we show the temperature profile for the first ~ 16 days of the mission. It can be seen that the He bath temperature was heading down to about 1.12 K before the main shell pump-out valve, V12, was opened on day 16.

On day 11 of the mission, the first ADR cycle was successfully conducted. The ADR cycle was initiated during a real time pass to verify that it had started properly, and then the cycle was allowed to continue during the next orbit. Upon acquisition during the subsequent pass, it was found that the ADR system was locked in tight temperature control at 60 mK.

A total of seven ADR cycles were run before the liquid helium was exhausted. Due to various tests and problems with early spacecraft operations and eventually with the liquid He cryogen, none of these ran to completion, but two ran normally for more than 23 hours, and the extensive data taken during ground tests could be used to reliably extrapolate these results to full cycles. The hold time was about 25% longer than on the ground, largely due to lower cryogen temperatures resulting from radiative cooling of the Dewar main shell to ~ 250 K. All aspects of the ADR on-orbit performance exceeded design goals, as shown in table 10.

As shown in figure 34, the neon temperatures decreased to ~ 15 K, which is lower than

Table 10. On-orbit ADR performance

Regulating temperature	60.0 mK
Temperature fluctuations	1.7 μK_{rms}
Long-term stability	< 1 μK
Hold time at 60 mK	38 hours
Recycle time	49 minutes
Operational duty cycle	97.9%
Heat load to LHe/recycle	21.0 J
FAA ordering*	12.3 J
Gas gap heat switch heater	2.9 J
Magnet hysteresis and eddy current heating†	5.8 J
Average heat load from ADR (38 h cycle)	154 μW
Average heat load from ADR (24 h cycle)‡	187 μW
LHe lifetime with 24 h cycle	3.9 years

Notes.

* The ordering energy scales with the length of the previous cycle.

† According to tests done on the Astro-E magnet, this is dominated by hysteresis losses [———ref]. It amounts to about 0.2% of the stored B field energy.

‡ We assume most recycles would be done early for convenience in scheduling. Effective duty cycle would still exceed 98% if slews and SAA passages are scheduled into recycle time.

the requirement of 17 K. On July 11, the mechanical cooler was turned on, just one day after launch. The operating power was increased in several steps, reaching the full power of 34.7 W on July 21. After the cooler was successfully put into operation, the VCS temperatures started decreasing, and reached 96 K on July 25 (see figure 35). The temperature of the main shall surface was 248 K at that time, very close to the anticipated value of 250 K, verifying that the Dewar surface and radiator panel worked as designed.

Figure 36 shows the calculated heat flow based on the inflight temperature history before V12 open on July 25. The total heat input to the Ne tank was 172 mW, and the expected lifetime of solid neon was 3.34 years. Therefore, we demonstrated that the Dewar survived the launch environment and achieved the thermal performance in orbit which could achieve its design goal of greater than three years.

Once V12 was opened on July 25, it was immediately apparent that internal Dewar temperatures began to change in an unexpected manner. The OVCS and MVCS began to warm while the IVCS cooled more rapidly. The Ne shroud showed a sudden drop in temperature

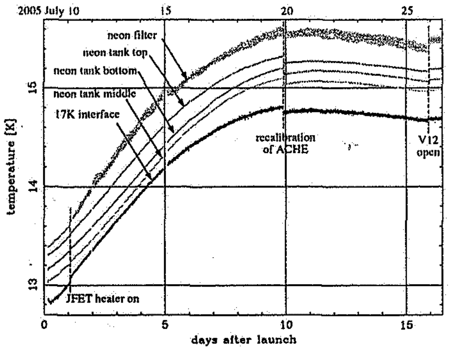

Fig. 34. Temperature history of the Ne tank (top, middle, bottom), the 17 K interface, and the Ne filter, from launch to the loss of helium.

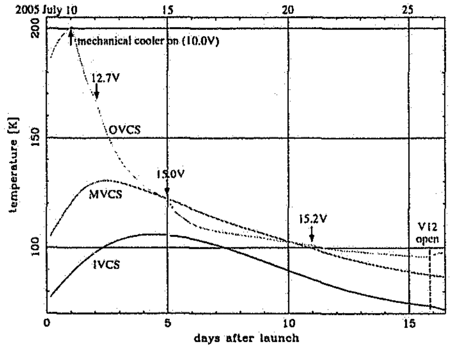

Fig. 35. Temperature history of IVCS, MVCS, and OVCS, from launch to the loss of helium.

while sensors on the He Cryostat exhibited a reverse trend and started warming. It was quickly realized that these profiles were all consistent with gas entering the Dewar guard vacuum and thermally shorting out the isolated components within the Dewar. All three of the Dewar vent valves are located interior to the spacecraft, and it is now considered all but certain that the spacecraft venting area is not large enough to prevent a significant flow impedance out to space. With the He and Ne vent gasses as a source, along with the expected outgassing of spacecraft materials, the interior spacecraft pressure, and thus Dewar guard vacuum pressure, are not sufficiently low enough to prevent gas conduction and adsorption within the Dewar. The likely partial pressures of He and Ne are estimated to be 10^{-6} and 10^{-5} torr, respectively, assuming a probable spacecraft vent area of 0.1 m^2. The pressure would have to have been at least three orders of magnitude lower in order not to be a significant heat load term on the He Cryostat ($\sim$ 25 μW). In principal, the charcoal getter on the He tank should have absorbed enough He to last $\sim$ 6 (???) months, but it is likely that the Ne gas that was also entering the Dewar significantly reduced the adsorption capacity of the getter. This situation resulted in the complete loss of liquid He on 2005 August 8, about 29 days after launch.

But before the He was completely exhausted, it was possible to successfully operate the microcalorimeter array and demonstrate its performance in space, along with the associated readout electronics.

10.2. Detector System

10.2.1. Energy resolution and gain stability

The XRS calorimeter operated in orbit long enough to obtain spectral data from the calibration pixel and briefly from the whole array using the filter-wheel source. The anti-coincidence detector became operational as soon as the electronics were powered and is still functioning. Background data on the array were also analyzed.

The calorimeter gain was extremely stable, needing only minor correction for drift even after cycling the ADR and after passage through the SAA. The effect from SAA passages appeared to be due to particle heating of the control thermometer during several intervals of satellite safe hold during which the ADR was cold but not regulated, the control thermometer reading increased during passage through the center of the SAA. Figure 37 is a gain history plot from the first 24-hour period after the first ADR cycle. The data gaps represent the SAA crossings. The XRS was operated through SAA passage, but the dead time from the high particle flux in the SAA resulted in an absence of detected x-rays. The resulting gain-corrected resolution from that first 24-hour interval was 6.97 ± 0.04 eV on the calibration pixel, using both "high-res" and "mid-res" grade primary events (figure 38).

In order to evaluate the performance of the rest of the array, the filter wheel was rotated into a position that allowed x-rays from an ^{55}Fe source to pass through the Be window of the XRS gate valve. Due to the combination of multiple satellite safe holds in the early operation of

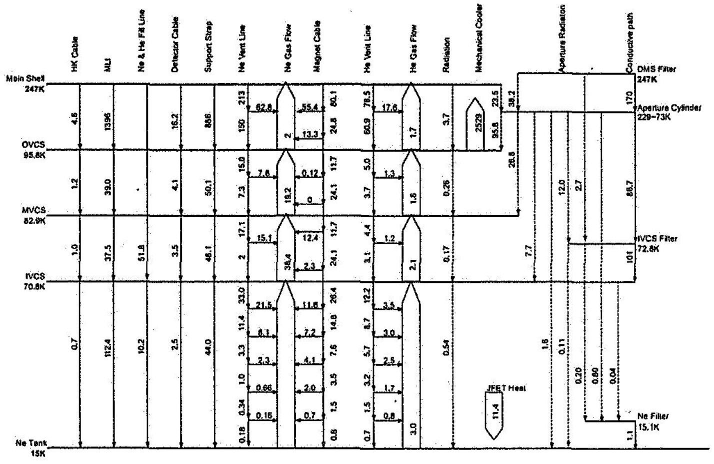

Fig. 36. Heat flow inside the Ne Dewar, based on in-orbit temperature history prior to opening V12. The mechanical cooler is operated at 35 W. All the numbers are in units of mW. The total heat input to the Ne tank is 172 mW, and the expected solid neon lifetime is 3.34 years.

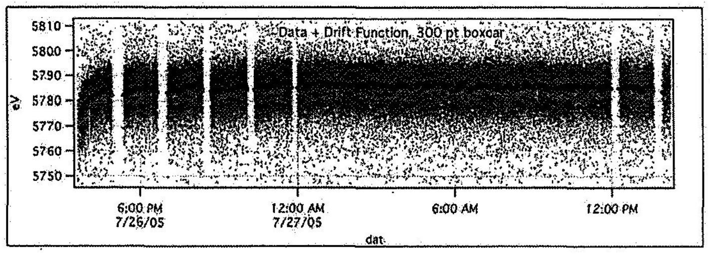

Fig. 37. Pulse height vs. time, showing the magnitude of the gain stability.

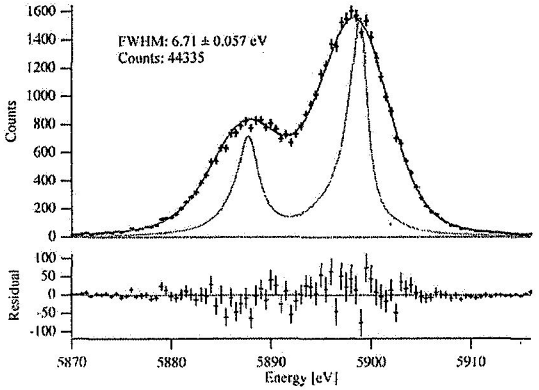

Fig. 38. In-flight, gain-corrected pulse height spectrum obtained from the data shown in Figure 35.

Suzaku and the early episodic effects of the helium in the XRS vacuum, there was only a 13-hour interval of good data while the filter-wheel source was in place. The composite resolution of the entire array during that interval was 7.82 ± 0.07 eV, with the resolution of all pixels (except the two known outliers) falling between 6.94 and 8.70 eV. The resolution of the calibration pixel was 7.19 ± 0.07 eV during the same time interval. Anomalous triggered events during this time interval indicated that even this integration was contaminated by He adsorption onto the calorimeter.

The slight degradation of the resolution in orbit from 6 eV to 7 eV appears to be another manifestation of the frame-heating effect. The resolution and noise of the calibration pixel were correlated with the particle rate measured by the anti-coincidence detector, as illustrated in figure 39. Before launch, the interaction of cosmic rays with the frame was seen as more of a problem for dead time instead of noise, since most cosmic rays produce events in the pixels that exceed the ~ 50-eV trigger threshold. After launch, we used two methods to estimate the spectrum of energy into the frame below the frame event threshold. In the first, we used a course anti-coincidence detector spectrum that had been determined by stepping its threshold, and we scaled this to that expected in the calorimeter frame assuming domination by minimum ionizing particles. In the second we used a GEANT simulation. Assuming that the NE^2 degradation determined for x-rays into the frame holds for 100–150 keV energy depositions, both estimates of the spectrum of energy deposited into the frame reproduce the resolution degradation observed, strongly supporting the hypothesis of noise from frame-heating by cosmic rays. Lowering the calorimeter pulse threshold would have ameliorated this effect to some extent, but the solution

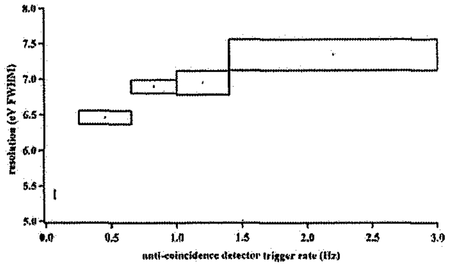

Fig. 39. Energy resolution vs. anticoincidence rate.

for a future mission will be to minimize the frame area and to improve heat sinking.

10.2.2. Background and operation of the anti-coincidence detector

The anticoincidence detector was operational for two weeks prior to the first ADR cycle, providing a preview of the particle background and allowing experimentation with the anti-coincidence threshold. Outside of the SAA, the measured rate ranged from 0.3 to 2 $c\,s^{-1}$ in the cm^2 detector, and the rate was inversely correlated with the geomagnetic cut-off rigidity, as expected. The threshold experiments showed that roughly half of the events deposit more than 430 keV (the highest setting for the threshold). Thus the spectrum is much harder than expected for minimum ionizing particles alone, for which 80% of the events would have been below 430 keV. A preliminary attempt to simulate secondary particles using a GEANT model made the spectrum somewhat harder, but still did not match the data.

We evaluated the XRS instrument background with the gate valve closed in a continuous 37103 s interval between crossings of the SAA. The science array experienced 850366 valid triggers between 0.1 and 12 keV in the 30 pixels. To identify pulses from frame events, we used a simple algorithm developed from analysis of the ground background data; this algorithm uses a single correlation interval of 0.5 ms and rejects groups of correlated events of as few as two events. The calibration pixel is included in the screening for correlated events because electrons that escape upon x-ray absorption in the calibration pixel can be detected on the main array (Kilbourne et al. 2006). More sophisticated screening that would, among other tests, consider the energy of the calibration pixel events and use a shorter coincidence window for pairs, would minimize dead time without sacrificing the effectiveness of the screening, but this software was not developed. After removing events within 0.5 ms of another event and events with the anti-coincidence flag, we had 207 events remaining. This corresponds to a rate of 5×10^{-2} $c\,s^{-1}\,cm^{-2}$ (0.1–12 keV). The spectrum of the background events (excluding low-resolution events, which removes 14 events) is shown in figure 40; there are no lines apparent with these statistics. The average rate in the anti-coincidence detector during that time interval was 0.9 $s^{-1}\,cm^{-2}$. If this

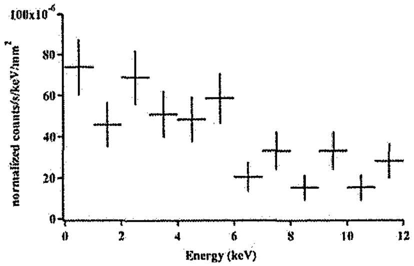

Fig. 40. XRS residual background rate

rate were generated by minimum ionizing particles, then the background rate in the calorimeter after applying the anti-coincidence veto would be 9×10^{-4} $c\,s^{-1}\,cm^{-2}$, so the measured residual background is dominated by secondary particles, as expected. The rate of frame events (for which one group of correlated calorimeter pulses is considered a single event) also works out to 0.9 $s^{-1}cm^{-2}$ of frame area, though the different effective thresholds and the shielding of the anti-coincidence detector by the calorimeter chip make it unlikely that the two rates refer precisely to the same population of events.

Another view of the particle environment is provided by counting all events that involve direct deposition of energy in a calorimeter absorber and the anti-coincidence detector. Because there is a narrow acceptance angle for incident particles to hit an absorber and the anti-coincidence detector but not the calorimeter frame, we must identify the frame events that also contain a pulse from a direct absorber hit. This is easily done by taking the ratio of the biggest pulse to the second-biggest pulse in a frame event cluster. The pulses of most frame events are similar in energy, but there is a distinct population for which the biggest pulse is greater than six times the height of the next biggest pulse. Tallying the veto-flagged events among these pulses and the isolated pulses (making no energy cuts) results in a rate of 0.55 $c\,s^{-1}cm^{-2}$. Even this rate is likely to be dominated by high-energy secondary particles because the range in cut-off rigidity sampled by the *Suzaku* orbit should have reduced the 1 $c\,s^{-1}\,cm^{-2}$ primary cosmic ray rate (in low earth orbit in a flat detector at solar minimum) by more than a factor of five. More sophisticated GEANT models are needed to understand the nature of the secondary particles and what future designs could be implemented to reduce the residual instrument background.

10.3. Detector Housing and Electronics

In-flight performance of FEA to go here

11. Summary

Although the short life span of the XRS is obviously a setback for celestial x-ray spectroscopy, it is hopefully a temporary one, and future implementations of this technology will benefit from the design an performance of the *Suzaku*/XRS.

Acknowledgments

The authors are extremely grateful to a hundreds of technicians, engineers, scientists, managers and students that have made the XRS possible. These include team members that contributed to the original design of the XRS and all of the efforts to successfully propose for and develop the XRS on *Suzaku*. In particular, we are extremely grateful for the significant contributions of the following team members:

NASA/Goddard Space Flight Center: Gustave Comeyne, Bernie Klein, John Leon, Dino Machi, Don Margolies and James Murphy for their management the XRS instrument.

Charlie Adams, Lorella Angelini, Dale Arbogast, Keith Arnaud, Shanta Arur, Bob Baker, Chris Baluta, Christine Baxley, Jason Behr, Tom Bialas, John Bichell, Dave Bloom, Regis Brekosky, Stephen Buchner, Ed Canavan, Phil Chen, Chuck Chidekel, Ron Colvin, Tony Comberiate, Jeff Condron, Tom Corris, Allen Crane, John Crow, Steve Derdeyn, Norm Dobson, Jeff Dumonthier, Mitra Dutta, Ken Ebisawa, Robert Edmonds, Rick Eichen, Dino Fasce, Enectali Figueroa-Feliciano, Charlie Fleetwood, Mike Flick, John Francis, Massimiliano Galeazzi, Joe Generie, Chris Gonzalez, Walt Goodale, Phil Goodwin, Marsha Gosselin, Steve Graham, Darrell Gretz, Fred Gross, John Gygax, Tom Hait, Christina Hammock, Chuck Hanchak, Holly Hancock, Tom Hanyok, Steven Harper, Ilana Harrus, John Harvey, Dave Huff, Nino Ingegneri, Sandra Irish, Harold Isenberg, Cliff Jackson, Mindy Jacobson, John Kearney, Linda Kearney, Jonathan King, Ron Kolecki, Michelle Lacombe, Juli Lander, Mike Lenz, Dahai Liu, Jim Lochner, James Loughlin, Ron Martin, Richard McClanahan, Leo McConville, Chris Miller, Christine Miranda, Herb Mittlemman, Anna Montoro, Theo Muench, Koji Mukai, Scott Murphy, Richard Mushotzky, Philip Myers, Son Ngo, Curtis Odell, Jeanne Palmer, Bill Pence, Frank Peters, Rob Petre, Ed Pier, Veronica Ponce, Ed Quinn, Joe Radich, John Rauscher, Marco Rosales, Brian Ross, Mike Ryschkewitsch, Tarek Saab, Carol Sappington, Sandy Schumann, Sharon Seiple, Noman Siddiqi, Ken Simms, Randall Smith, Carl Stahle, Darrell Story, John Sutton, Louis Thomas, David Turnbo, Jim Tuttle, Brent Warner, Nicholas White, Crystal White, Maxine Windhausen, George Winkert, George Wofford, Steve Wood, Gerry Wright, Debbie Yodder and John Zahniser for designing, building and providing guidance to the XRS hardware and science program.

Department of Physics, University of Wisconsin: Nick Bilgri, Ethan Feldman, Lindsay Rocks, Wilt Sanders, John Vaillancourt and Gaudenis Vidugiris for the development of the flight internal calibration source and contributions to the microcalorimeter design.

Space Science Engineering Center, University of Wisconsin: Bob Paulos for overseeing and providing rapid delivery of the ADR saltpill.

Luxel Corporation: Forbes Powell for working closely with Goddard to develop the x-ray blocking filters.

NASA Headquarters: Drs. Alan Bunner, Paul Hertz and Louis Kaluzienski for their efforts to make the XRS and the Suzaku program a reality, and their continuous support of the Suzaku US Guest Investigator Program. Also Steve Horowitz, Adriana Ocampo and Alan Smale for program and international support.

ISAS/JAXA: Prof. Kenji Minesugi at ISAS/JAXA for mechanical design of the neon dewar.

Sumitomo Heavy Industries, Ltd.: Makoto Kyoya, Seiji Yoshida, Keisuke Tsurumi, Yoshiyuki Kimura, Takeshi Hiroishi, Isao Gonda, Yoshinobu Ochi, Yumiki Ochi, Yuji Tarumi, Junji Seno, Kenji Okamoto, Shoji Tsunematsu, Shunji Hoshika, Kiyomi Otsuka, Yoji Fujioka, Jun'ichi Inoue, Shizuo Miyawaki, Norihisa Itoh, Sanae Takahashi for fabrication and testing of the dewar.

NEC Toshiba Space Systems, Ltd.: Kenji Kitade, Takayuki Tohma, Kazuyo Mizushima for the spacecraft interface and overall testing on spacecraft, Teiji Yoshida, Toshimitsu Nakayama for facrication of the power supply unit, and Akira Fukatsu, Takuji Nakano, Taku Saito, Hiroaki Nishio, Hideki Takei for fabrication of the filter wheel.

Fujitsu, Inc.: Keiji Satoh, Kohji Hayashi, Keitaro Ohno for fabrication of Astro-E XRS-DE.

Mitsubishi Heavy Industries, Ltd.: Naoki Shibayama, Makio Yamaguchi, Atsushi Nakajima, Kazunori Masukawa, Keigo Sasou, Shigeo Kasai for fabrication of Astro-E2 XRS-DE.

SHI Examination & Inspection, Ltd.: Akira Nagano for fabrication of ^{41}Ca source.

Takeshi Toramatsu, Akira Hayakawa, Chiaki Inoue at Tokyo Metropolitan University for calibration of the filter wheel, and Toshiyuki Miyazaki, Tai Oshima, Masahiro Yamazaki, Akihiro Kushino, Teru Ishikawa, Yuichiro Ezoe, Kiyonori Yoshida, Akihiro Tsuchiya, Kensuke Masui, Tomotaka Yoshino, Toshishige Hagihara, Kosuke Sato, Tamayuki Fujimori, Akio Hoshino, Yoshiyuki Yamakawa, and post-docs/graduate students at ISAS/JAXA and Tokyo Metropolitan University who supported testing and monitoring of the dewar for a long time until launch.

References

Bavdaz, M., Lumb, D., Gerlach, L., Parmar, A., & Peacock, A. 2005, Proc. SPIE, 5898, 57
Boyce, K. R., et al. 1999, Proc. SPIE, 3765, 741
Brekosky, R. P., et al. 2004, NIM A 520, 439
Brinkman, A. C., et al. 2000, ApJ, 530, L111

Canizares, C. R., et al. 2000, ApJ, 539, L41

Cottam, J., et al. 2004, NIM A, 520, 368

Cottam, J., et al. 2006, NIM A, 559, 617

Fujimoto, R., Mitsuda, K., Hirabayashi, M., Narasaki, K., Breon, S., Boyle, R., DiPirro, M., Volz, S. M., Kelley, R. L. 2006, NIM A, 559, 648

Furusho, T., et al. 1999, Proc. SPIE 3765, 664

Gendreau, K. C. 1995, Ph.D. thesis, Massachusetts Institute of Technology

Germire, G. P. 1999, BAAS, 31, 1515

den Herder, J. W., et al. 2001, A&A, 365, L7

Jansen, F., et al. 2001, A&A, 365, L1

Kilbourne, C. A., et al. 2006, NIM A 559, 620

Han, S.-I., et al. 1998, Proc. SPIE, 3445, 640

Koyama, K., et al. 2006, this volume

Ota, N., et al. 2006, NIM A, 559, 614

McCammon, D. et al. 2002, ApJ, 576, 188

McCammon, D. 2005, LTD Book,

Mitsuda, K., et al. 2006, this volume

Moseley, S. H., Mather, J. C., & McCammon, D. 1982, Journal of Ap. Phys., 56, 1257

Narasaki, K., et al. 2006, Adv. Cryo. Eng. 51, 1505

Nagamatsu, J., Nakagawa, N., Muranaka, T., Zenitani, Y., & Akimitsu, J. 2001, Nature, 410, 63

Neugebauer, G., et al. 1984, ApJ, 278, L1

Saab, T., et al. 2004, Proc. SPIE, 5505, 320

Serlemitsos, A. T., Warner, B. A., Sansebastian, M., & Kunes, E. 1990, Proc SPIE, 1340, 303

Serlemitsos, P. J., et al. 1995, PASJ, 47, 105

Serlemitsos, P. J., et al. 2006, this volume

Shirron, P. J., DiPirro, M. J., Panek, J., Kelley, R., Mitsuda, K, Fujimoto, R., Hirabayashi, M., & McCammon, D. 2006, NIM A, 559, 666

Stahle, C. K., et al. 1999, Proc. SPIE, 3765, 128

Stahle, C. K., et al. 2003, Proc. SPIE, 4851, 1394

Stahle, C. K., McCammon, D., and Irwin, K. D. August 1999, Physics Today, p.32

Strüder, L., et al. 2001, A&A, 365, L18

Takahashi, T., Mitsuda, K., & Kunieda, H. 2006a, Proc. SPIE, 6266, 62660D

Takahashi, T., et al. 2006b, this volume

Turner, M. L. J., et al. 2001, A&A, 365, 27L

Volz, S. M., et al. 1996, Cryogenics, 36, 763

Weisskopf, M. C., Brinkman, B., Canizares, C., Garmire, G., Murray, S., & van Speybroeck, L. P. 2002, PASP, 114, 1